REPORT 1231

NACA TRANSONIC WIND-TUNNEL TEST SECTIONS[1]

By Ray H. Wright and Vernon G. Ward

SUMMARY

An approximate subsonic theory was developed for the solid-blockage interference in circular wind tunnels with walls slotted in the direction of flow. This theory indicated the possibility of obtaining zero blockage interference. Tests in a circular slotted tunnel based on the theory confirmed the theoretical predictions.

The slotted wind tunnel was operable at supersonic speeds merely by increasing the power input, and moreover, the supersonic Mach number produced could be varied by varying the power. The phenomenon of choking, characteristic of closed tunnels, did not occur in the slotted tunnel.

Comparison of pressure measurements on a practical size nonlifting model in the slotted tunnel with measurements obtained on the same model in a much larger closed tunnel, in which the interference effects were negligible, showed good agreement at subsonic Mach numbers not greatly exceeding the critical and fair agreement over most of the model surface at Mach numbers up to 1.1.

The transonic operation of this type of test section requires considerable further experimentation and analysis.

INTRODUCTION

Model testing in wind tunnels at high subsonic Mach numbers presents special difficulties that increase in severity as Mach number 1.0 is approached. To obviate tunnel choking and severe interference effects due to constriction of solid walls in closed wind tunnels, the model size must be continuously decreased as the Mach number approaches unity from either direction so that at Mach numbers near unity, vanishingly small models are required. This requirement prevents, in closed wind tunnels, a study of model characteristics continuously through the sonic region. It was recognized that open-throat tunnels, because of their constant pressure boundary, could not permit the existence of the strong axial pressure gradients characteristic of choked closed-throat tunnels. In fact, the very first efforts to construct high-speed wind tunnels were made by use of open-throat tunnels. Large power requirements and flow unsteadiness of open-throat tunnels at high Mach numbers, however, interposed serious disadvantages, and thus closed-throat tunnels were employed. As the need for adequate research facilities for the range of Mach number near and through 1.0 grew, new efforts were instituted to solve the problem of wind-tunnel testing limitations for the Mach number 1.0 region. Fundamental considerations of the problem of wind-tunnel-wall corrections and choking limitations led to the idea of a "porous wall."

Theoretical consideration of the problem with subsonic flow indicated the possibility of reducing the interference due to boundaries by means of slots in the solid boundary extending in the direction of flow. On the basis of approximate theoretical results, such a slotted wind tunnel was designed. Tests of a model in this slotted wind tunnel indicated that the primary object of minimizing the interference effects due to constriction had been attained. At the same time, the tests showed that the slotted test section could be operated continuously through the transonic range to low supersonic Mach numbers without change in tunnel configuration. No theory has yet been developed for upper transonic and supersonic operation. The subsonic theory was first developed in useful form in September 1946. This report presents the significant research results obtained to date.

SUBSONIC THEORY

The first investigation undertaken in this project was a theoretical study of the solid blockage in a wind tunnel with cylindrical boundary containing open slots parallel to the flow. It was thought possible, since the interference velocities due to the boundaries are of opposite signs with free and solid boundaries, that the opposite effects might be so combined in a slotted tunnel as to produce zero solid blockage. The theoretical development follows.

Consider a doublet placed on the axis of a circular slotted wind tunnel (fig. 1). On the assumption of incompressible potential flow, the potential due to this doublet is

$$\phi=\frac{m}{4\pi}\frac{x}{\sqrt{(x^2+r^2)^3}} \tag{1}$$

where

m doublet strength

x coordinate in axial direction

r radial coordinate

The total disturbance potential within the tunnel is assumed to be given by the sum of the doublet potential ϕ and a disturbance potential ϕ^* determined from the following boundary conditions:

At the slots

$$[\phi+\phi^*]_{r=R}=0 \tag{2}$$

[1] Supersedes NACA RM L8J06, 1948.

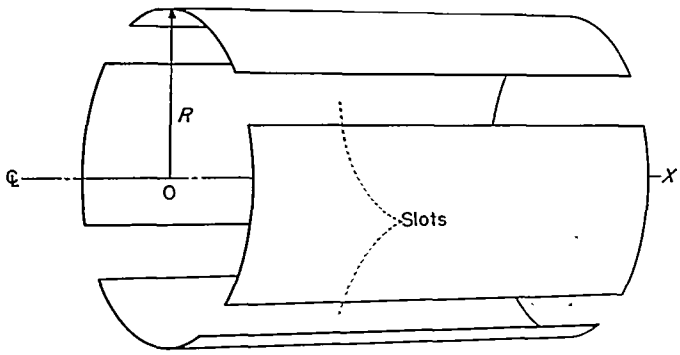

FIGURE 1.—Circular slotted wind-tunnel configuration.

At the solid boundaries

$$\left[\frac{\partial(\phi+\phi^*)}{\partial r}\right]_{r=R}=0 \tag{3}$$

where R is the tunnel radius. The perturbation potential ϕ^*, like ϕ, must satisfy Laplace's equation. Thus, in cylindrical coordinates

$$\frac{\partial^2\phi^*}{\partial r^2}+\frac{1}{r}\frac{\partial\phi^*}{\partial r}+\frac{1}{r^2}\frac{\partial^2\phi^*}{\partial\theta^2}+\frac{\partial^2\phi^*}{\partial x^2}=0 \tag{4}$$

where θ is the angular coordinate as indicated in figure 2. Let n slots be spaced symmetrically in the boundary. It is then possible and convenient to treat the flow in only one of the n identical sectors produced by drawing radii to the centers of the n open segments of the boundary. (See fig. 2.) With the transformation

$$\omega=n\theta \tag{5}$$

ω covers a range of 2π in each sector. Moreover, if the origin for ω is taken at the radius drawn to the center of the closed segment, the range 0 to $-\pi$ is seen to be exactly symmetrical to the range 0 to π, so that only the positive values of ω in the range 0 to π need be considered. With the transformation (5), equation (4) becomes

$$\frac{\partial^2\phi^*}{\partial r^2}+\frac{1}{r}\frac{\partial\phi^*}{\partial r}+\frac{n^2}{r^2}\frac{\partial^2\phi^*}{\partial\omega^2}+\frac{\partial^2\phi^*}{\partial x^2}=0 \tag{6}$$

From symmetry, as may be seen from figure 2, the boundary conditions

$$\left[\frac{\partial\phi^*}{\partial\omega}\right]_{\omega=0}=\left[\frac{\partial\phi^*}{\partial\omega}\right]_{\omega=\pi}=0 \tag{7}$$

apply. The use of the finite Fourier cosine transformation with respect to ω is therefore suggested. (See ref. 1.) Application of the finite cosine transform to equation (6) and to the boundary conditions (2) and (3), with consideration of equation (7), yields

$$\frac{\partial^2\varphi_c}{\partial r^2}+\frac{1}{r}\frac{\partial\varphi_c}{\partial r}-\frac{n^2s^2}{r^2}\varphi_c+\frac{\partial^2\varphi_c}{\partial x^2}=0 \tag{8}$$

$$[\varphi_c]_{r=R}=[-\phi]_{r=R}\left[\frac{\sin(s\pi)-\sin(s\omega_1)}{s}\right]+\int_0^{\omega_1}[\phi^*]_{r=R}\cos(s\omega)\,d\omega \tag{9}$$

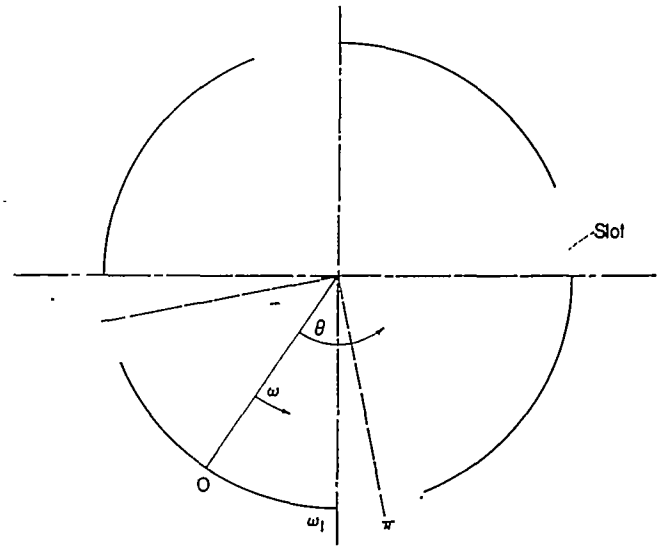

FIGURE 2.—Cross section showing slots and angle relations. $\omega=n\theta$. For case shown, $n=4$.

$$\left[\frac{\partial\varphi_c}{\partial r}\right]_{r=R}=\left[-\frac{\partial\phi}{\partial r}\right]_{r=R}\left[\frac{\sin(s\omega_1)}{s}\right]+\int_{\omega_1}^{\pi}\left[\frac{\partial\phi^*}{\partial r}\right]_{r=R}\cos(s\omega)\,d\omega \tag{10}$$

where φ_c is the finite cosine transformation of ϕ^* with respect to ω and is given by

$$\varphi_c(r,x,s)=\int_0^{\pi}\phi^*\cos(s\omega)\,d\omega \tag{11}$$

and $s=0, 1, 2, 3, \ldots$. Equation (9) is obtained under the consideration that

$$[\phi^*]_{r=R}=[-\phi]_{r=R}+[\phi^*]_{r=R}$$
$$\omega_1\leq\omega\leq\pi \quad 0\leq\omega\leq\omega_1$$

where ω_1 is the value of ω at the edge of the slot. A similar consideration applies to equation (10). The assumption is now made that equation (8) can be solved by the method of separation of variables. Thus, let

$$\varphi_c(r,x,s)=X(x)\,P(r,s) \tag{12}$$

Use of equation (12) in equation (8) gives

$$XP_{rr}+\frac{1}{r}XP_r-\frac{n^2s^2}{r^2}XP+PX_{xx}=0 \tag{13}$$

where the subscripts r and x indicate derivatives with respect to those variables. Division of equation (13) by XP gives

$$\frac{P_{rr}}{P}+\frac{1}{r}\frac{P_r}{P}-\frac{n^2s^2}{r^2}+\frac{X_{xx}}{X}=0 \tag{14}$$

Since the sum of the first three terms of this equation is independent of x and the last term is independent of r and s

$$\frac{X_{xx}}{X}=\text{Some Quantity Independent of } x,\ r, \text{ and } s$$
$$=-\gamma^2 \tag{15}$$

where γ is to be considered a parameter that may be varied at will. The solution with respect to the variable x is the same as that obtained in reference 2. Equation (15) is solved by terms of the type

$$X_\gamma = A_\gamma \sin \gamma x \tag{16}$$

where A_γ is a constant for any given value of γ and solutions may be added to obtain a function of x satisfying the boundary conditions. For the variable r, use of equation (15) in equation (14) and multiplication by P gives

$$P_{rr} + \frac{P_r}{r} - \left(\frac{n^2 s^2}{r^2} + \gamma^2\right) P = 0 \tag{17}$$

or

$$\gamma^2 r^2 P_{(\gamma r)(\gamma r)} + \gamma r P_{\gamma r} - (n^2 s^2 + \gamma^2 r^2) P = 0 \tag{18}$$

A solution of equation (18) is

$$P = B_{ns} I_{ns}(\gamma r) \tag{19}$$

where B_{ns} is a constant for any given value of ns, and I_{ns} is the modified Bessel function of the first kind. (See ref. 3, chapter III.) The corresponding function of the second kind fails to appear because of the necessity that the solution be regular within the tunnel. Now write

$$\gamma = \frac{k\pi}{l} \qquad (k = 1, 2, 3, \ldots) \tag{20}$$

where l is the x-length over which X is to be defined. Then equation (16) becomes

$$X_k = A_k \sin \frac{k\pi x}{l} \tag{21}$$

and equation (12) becomes

$$\varphi_c(r,x,s) = \sum_{k=1}^{\infty} A_k B_{ns} I_{ns}\left(\frac{k\pi r}{l}\right) \sin \frac{k\pi x}{l} \tag{22}$$

Also, from reference 1,

$$\begin{aligned}\phi^* &= \frac{1}{\pi}\varphi_c(r,x,0) + \frac{2}{\pi}\sum_{s=1}^{\infty} \varphi_c(r,x,s)\cos(s\omega) \\ &= \frac{1}{\pi}\sum_{k=1}^{\infty} A_k B_0 I_0\left(\frac{k\pi r}{l}\right)\sin\left(\frac{k\pi x}{l}\right) + \\ &\quad \frac{2}{\pi}\sum_{s=1}^{\infty} B_{ns}\cos(s\omega)\sum_{k=1}^{\infty} A_k I_{ns}\left(\frac{k\pi r}{l}\right)\sin\left(\frac{k\pi x}{l}\right)\end{aligned} \tag{23}$$

and if, in equation (23), j is written instead of s

$$\begin{aligned}[\phi^*]_{r=R} &= \frac{1}{\pi}\sum_{k=1}^{\infty} A_k B_0 I_0\left(\frac{k\pi R}{l}\right)\sin\left(\frac{k\pi x}{l}\right) + \\ &\quad \frac{2}{\pi}\sum_{j=1}^{\infty} B_{nj}\cos(j\omega)\sum_{k=1}^{\infty} A_k I_{nj}\left(\frac{k\pi R}{l}\right)\sin\left(\frac{k\pi x}{l}\right)\end{aligned} \tag{24}$$

and

$$\begin{aligned}\left[\frac{\partial\phi^*}{\partial r}\right]_{r=R} &= \frac{1}{\pi}\sum_{k=1}^{\infty}\frac{k\pi}{l} A_k B_0 I_0'\left(\frac{k\pi R}{l}\right)\sin\left(\frac{k\pi x}{l}\right) + \\ &\quad \frac{2}{\pi}\sum_{j=1}^{\infty} B_{nj}\cos(j\omega)\sum_{k=1}^{\infty}\frac{k\pi}{l} A_k I_{nj}'\left(\frac{k\pi R}{l}\right)\sin\left(\frac{k\pi x}{l}\right)\end{aligned} \tag{25}$$

where the primes indicate derivatives with respect to the arguments of the Bessel functions. From equation (22)

$$[\varphi_c]_{r=R} = \sum_{k=1}^{\infty} A_k B_{ns} I_{ns}\left(\frac{k\pi R}{l}\right)\sin\left(\frac{k\pi x}{l}\right) \tag{26}$$

$$\left[\frac{\partial\varphi_c}{\partial r}\right]_{r=R} = \sum_{k=1}^{\infty}\frac{k\pi}{l} A_k B_{ns} I_{ns}'\left(\frac{k\pi R}{l}\right)\sin\left(\frac{k\pi x}{l}\right) \tag{27}$$

Suppose also that $[\phi]_{r=R}$ and $\left[\frac{\partial\phi}{\partial r}\right]_{r=R}$ are expanded in Fourier series with $\sin\frac{k\pi x}{l}$, so that

$$[\phi]_{r=R} = \sum_{k=1}^{\infty} Q_{k_1}\sin\left(\frac{k\pi x}{l}\right) \tag{28}$$

$$\left[\frac{\partial\phi}{\partial r}\right]_{r=R} = \sum_{k=1}^{\infty} Q_{k_2}\sin\left(\frac{k\pi x}{l}\right) \tag{29}$$

where Q_{k_1} and Q_{k_2} are the constants. The boundary condition (9) now becomes, by use of equations (24), (26), and (28):

$$\begin{aligned}\sum_{k=1}^{\infty} A_k B_{ns} I_{ns}\left(\frac{k\pi R}{l}\right)\sin\left(\frac{k\pi x}{l}\right) &= -\left[\frac{\sin(s\pi)-\sin(s\omega_1)}{s}\right]\sum_{k=1}^{\infty} Q_{k_1}\sin\left(\frac{k\pi x}{l}\right) + \\ &\quad \frac{1}{\pi}\sum_{k=1}^{\infty} A_k B_0 I_0\left(\frac{k\pi R}{l}\right)\sin\left(\frac{k\pi x}{l}\right)\int_0^{\omega_1}\cos(s\omega)\,d\omega + \frac{2}{\pi}\sum_{k=1}^{\infty} A_k \sin\left(\frac{k\pi x}{l}\right)\sum_{j=1}^{\infty} B_{nj} I_{nj}\left(\frac{k\pi R}{l}\right)\int_0^{\omega_1}\cos(j\omega)\cos(s\omega)\,d\omega\end{aligned}$$

and the boundary condition (10) becomes, by use of equations (25), (27), and (29):

$$\begin{aligned}\sum_{k=1}^{\infty}\frac{k\pi}{l} A_k B_{ns} I_{ns}'\left(\frac{k\pi R}{l}\right)\sin\left(\frac{k\pi x}{l}\right) &= -\left[\frac{\sin(s\omega_1)}{s}\right]\sum_{k=1}^{\infty} Q_{k_2}\sin\left(\frac{k\pi x}{l}\right) + \\ &\quad \frac{1}{\pi}\sum_{k=1}^{\infty}\frac{k\pi}{l} A_k B_0 I_0'\left(\frac{k\pi R}{l}\right)\sin\left(\frac{k\pi x}{l}\right)\int_{\omega_1}^{\pi}\cos(s\omega)\,d\omega + \frac{2}{\pi}\sum_{k=1}^{\infty}\frac{k\pi}{l} A_k \sin\left(\frac{k\pi x}{l}\right)\sum_{j=1}^{\infty} B_{nj} I_{nj}'\left(\frac{k\pi R}{l}\right)\int_{\omega_1}^{\pi}\cos(j\omega)\cos(s\omega)\,d\omega\end{aligned}$$

Equating coefficients of $\sin\left(\frac{k\pi x}{l}\right)$ and performing the indicated integrations gives

$$A_k B_{ns} I_{ns}\left(\frac{k\pi R}{l}\right) = -Q_{k_1}\left[\frac{\sin(s\pi)-\sin(s\omega_1)}{s}\right] + \frac{A_k B_0}{\pi} I_0\left(\frac{k\pi R}{l}\right)\frac{\sin(s\omega_1)}{s} + \frac{2}{\pi} A_k \sum_{j=1}^{\infty} B_{nj} I_{nj}\left(\frac{k\pi R}{l}\right)\left[\frac{\sin(j-s)\,\omega_1}{2(j-s)} + \frac{\sin(j+s)\,\omega_1}{2(j+s)}\right] \tag{30}$$

and

$$\frac{k\pi}{l} A_k B_{ns} I_{ns}'\left(\frac{k\pi R}{l}\right)=-Q_{k_2}\left[\frac{\sin(s\omega_1)}{s}\right]+\frac{kA_k}{l} B_0 I_0'\left(\frac{k\pi R}{l}\right)\left[\frac{\sin(s\pi)-\sin(s\omega_1)}{s}\right]+$$
$$\frac{2kA_k}{l}\sum_{j=1}^{\infty} B_{nj} I_{nj}'\left(\frac{k\pi R}{l}\right)\left[\frac{\sin(j-s)\pi-\sin(j-s)\omega_1}{2(j-s)}-\frac{\sin(j+s)\omega_1}{2(j+s)}\right] \tag{31}$$

In equations (23), (30), and (31) A_k, Q_{k_1}, Q_{k_2}, and the Bessel functions depend upon k, which takes on only integral values. In reference 2, however, the length l was extended to infinity and the Fourier series was replaced by a Fourier integral. With the integral form, the coefficients A_k, Q_{k_1}, and Q_{k_2} are replaced by continuous functions of k/l or, otherwise of

$$q=\frac{k\pi R}{l} \tag{32}$$

If, also,

$$\left.\begin{aligned}\frac{r}{R}&=\rho\\ \frac{x}{R}&=\xi\end{aligned}\right\} \tag{33}$$

and, if the functions $A(q)$ are combined with the coefficients B_{ns} or B_{nj}, equation (23) is replaced with

$$\phi^*=\frac{1}{\pi}\int_0^\infty C_0(q)\, I_0(q\rho)\sin(q\xi)\, dq+$$
$$\frac{2}{\pi}\sum_{s=1}^{\infty}\cos(s\omega)\int_0^\infty C_{ns}(q)\, I_{ns}(q\rho)\sin(q\xi)\, dq \tag{34}$$

and equations (30) and (31) with

$$C_{ns}(q)\, I_{ns}(q)=-Q_1(q)\left[\frac{\sin(s\pi)-\sin(s\omega_1)}{s}\right]+\frac{C_0(q)}{\pi} I_0(q)\frac{\sin(s\omega_1)}{s}+\frac{2}{\pi}\sum_{j=1}^{\infty} C_{nj}(q)\, I_{nj}(q)\left[\frac{\sin(j-s)\,\omega_1}{2(j-s)}+\frac{\sin(j+s)\,\omega_1}{2(j+s)}\right] \tag{35}$$

and

$$\frac{q}{R} C_{ns}(q)\, I_{ns}'(q)=-Q_2(q)\left[\frac{\sin(s\omega_1)}{s}\right]+\frac{q}{\pi R} C_0(q)\, I_0'(q)\left[\frac{\sin(s\pi)-\sin(s\omega_1)}{s}\right]+$$
$$\frac{2q}{\pi R}\sum_{j=1}^{\infty} C_{nj}(q)\, I_{nj}'(q)\left[\frac{\sin(j-s)\pi-\sin(j-s)\omega_1}{2(j-s)}-\frac{\sin(j+s)\omega_1}{2(j+s)}\right] \tag{36}$$

Since Q_1 and Q_2 are now the functions which when multiplied by $\sin(q\xi)$ make up the integrands in the Fourier integral expression of $[\phi]_{r=R}$ and $\left[\frac{\partial\phi}{\partial r}\right]_{r=R}$, respectively, consideration of equation (1) gives

$$Q_1(q)=\frac{m}{2\pi^2R^2}\int_0^\infty\frac{\xi}{\sqrt{(\xi^2+1)^3}}\sin(q\xi)\, d\xi \tag{37}$$

$$Q_2(q)=\frac{-m}{2\pi^2R^3}\int_0^\infty\frac{3\xi}{\sqrt{(\xi^2+1)^5}}\sin(q\xi)\, d\xi \tag{38}$$

Integration by parts and consideration of reference 4 shows that

$$Q_1(q)=\frac{m}{2\pi^2R^2} qK_0(q) \tag{39}$$

$$Q_2(q)=\frac{-m}{2\pi^2R^3} q^2K_1(q) \tag{40}$$

where K_0 and K_1 are modified Bessel functions of the second kind. If the equations (35) and (36) are solved for $C_{ns}(q)$ and if the right-hand sides are then equated to each other and the relations (39) and (40) are used, the following equation for determining the functions $C_{ns}(q)$ results:

$$\frac{C_0(q)}{\pi}\left\{\frac{I_0(q)}{I_{ns}(q)}\frac{\sin(s\omega_1)}{s}-\frac{I_0'(q)}{I_{ns}'(q)}\left[\frac{\sin(s\pi)-\sin(s\omega_1)}{s}\right]\right\}+\frac{2}{\pi}\sum_{j=1}^{\infty} C_{nj}(q)\left\{\frac{I_{nj}(q)}{I_{ns}(q)}\left[\frac{\sin(j-s)\omega_1}{2(j-s)}+\frac{\sin(j+s)\omega_1}{2(j+s)}\right]-\right.$$
$$\left.\frac{I_{nj}'(q)}{I_{ns}'(q)}\left[\frac{\sin(j-s)\pi-\sin(j-s)\omega_1}{2(j-s)}-\frac{\sin(j+s)\omega_1}{2(j+s)}\right]\right\}$$
$$=\frac{mq}{2\pi^2R^2}\left\{\frac{K_0(q)}{I_{ns}(q)}\left[\frac{\sin(s\pi)-\sin(s\omega_1)}{s}\right]+\frac{K_1(q)}{I_{ns}'(q)}\left[\frac{\sin(s\omega_1)}{s}\right]\right\} \tag{41}$$

For convenience, take

$$P_{nj}(q)\equiv P_{nj}=\left[\frac{\frac{qC_0(q)}{m}}{2\pi R^2}\right]_{j=0}=\left[\frac{\frac{qC_{nj}(q)}{m}}{4\pi R^2}\right]_{j\neq 0} \tag{42}$$

and let the argument q of the Bessel functions be understood. Then, since $I_0'=I_1$, equation (41) can be written, after some rearrangement and after multiplication with the product $I_{ns}I_{ns}'$

$$P_0\left\{[I_0 I_{ns}'+I_1 I_{ns}]\frac{\sin(s\omega_1)}{s}-I_1 I_{ns}\frac{\sin(s\pi)}{s}\right\}+\sum_{j=1}^{\infty}P_{nj}\left\{[I_{ns}I_{nj}'+I_{ns}'I_{nj}]\left[\frac{\sin(j-s)\omega_1}{2(j-s)}+\frac{\sin(j+s)\omega_1}{2(j+s)}\right]-I_{ns}I_{nj}'\left[\frac{\sin(j-s)\pi}{2(j-s)}\right]\right\}$$
$$=-q^2\left\{[I_{ns}'K_0-I_{ns}K_1]\frac{\sin(s\omega_1)}{s}-K_0 I_{ns}'\frac{\sin(s\pi)}{s}\right\}\qquad s=1,2,3\ldots \tag{43}$$

Equations (43) provide at each value of q an infinite system of simultaneous linear algebraic equations for the determination of the values of the functions $P_{nj}(q)$ at that point. With use of equation (42) the interference potential (34) can be written

$$\phi^*=\frac{m}{2\pi^2R^2}\sum_{s=0}^{\infty}\cos(s\omega)\int_0^{\infty}\frac{P_{ns}(q)}{q}I_{ns}(q\rho)\sin(q\xi)\,dq \tag{44}$$

from which the interference velocity in the direction of the tunnel axis is

$$u^*=\frac{m}{2\pi^2R^3}\sum_{s=0}^{\infty}\cos(s\omega)\int_0^{\infty}P_{ns}(q)\,I_{ns}(q\rho)\cos(q\xi)\,dq \tag{45}$$

It seems likely that, if the first few functions P_{ns} could be obtained, the interference velocities not only in the axial direction but also in the radial and angular directions (obtained by differentiating equation (44) with respect to radial and axial distances) could be satisfactorily expressed. Unfortunately, every function P_{ns} depends upon every other one according to equations (43) and even P_0 may therefore be very difficult to obtain with a sufficient degree of approximation. Some information may be obtained, however, from the form of the solution. On the axis of the tunnel ($\rho=0$), which is in the region of greatest interest because the model is located at the center, the interference velocity is determined by the function P_0 alone; for all the Bessel functions $I_{ns}(0)$ are zero except for $I_0(0)$, which is equal to unity. Moreover, as the argument is decreased, the value of the Bessel function I_{ns} decreases ever more strongly as the order is increased; therefore, if a value of ω_1 can be chosen such that the interference velocity at the tunnel axis is zero, the interference slightly off the axis will be less as the number of slots n becomes greater. In any case, the variation of interference velocity with angular position near the tunnel axis will be decreased by increasing the number of slots, since the interference corresponding to P_0 is invariant with respect to ω. The angular variation of the axial and radial velocities will be symmetrical about $\omega=0$. The angular interference velocities will be antisymmetrical about $\omega=0$. Since the only function of x appearing in equation (45) is the even function $\cos(q\xi)$, the variations of the axial velocities will be symmetrical about $x=0$ (the position of the doublet). The radial and angular variations, however, will be antisymmetrical about $x=0$.

The infinite integral appearing in equations (44) and (45) causes no trouble and can be graphically obtained, since it appears to converge in the region of $q=8$. For the closed tunnel ($\omega_1=\pi$) and for the open tunnel ($\omega_1=0$), for both of which P_{ns} is zero except for P_0 and for which P_0 degenerates to known functions of q including Bessel functions, this convergence has been proved through the use of asymptotic expansions of the Bessel functions.

The system of equations (43) has been set up in matrix form for 10 of the equations and 10 of the unknown functions $P_{nj}(q)$. (See table I.) For each row the value of s is constant; for each column the value of j is constant. The argument of the Bessel functions is q in every case. The determinant of the left side of equations (43) is contained in the space below and to the left of the double lines in table I. This determinant is symmetrical about a diagonal; squares containing identical quantities are indicated with identical numbers. In each square the function of Bessel functions is to be multiplied by the function of trigonometric functions appearing in that same square. The functions P_{nj} applying to their respective columns are given in the row above and to the left of the double lines. The K at the top of the column to the right of the double lines indicates that the column contains the constants given by the right-hand side of equations (43).

The system of equations (43) has not been shown to be convergent. The Fourier series in $\cos(s\omega)$ is required not only to express a function ϕ^* and its first and second derivatives but also to satisfy two simultaneous equations expressing two different kinds of boundary conditions. The boundary conditions are discontinuous at the edges of the slots ($\omega=\omega_1$), and, by analogy with thin airfoil theory, the velocities at the edges are expected to be infinite. Such boundary conditions cannot be exactly satisfied by a Fourier series and it would not be surprising, therefore, if the system

TABLE I

SCHEDULE FOR COMPUTATION OF THE CONSTANTS P_{nj} WITH TEN EQUATIONS

P_0	P_n	P_{2n}	P_{3n}	P_{4n}	P_{5n}	P_{6n}	P_{7n}	P_{8n}	P_{9n}	K
$2\omega_1-\pi$ (1) I_0I_1	$\sin\omega_1$ (2) $I_0I_n'+I_1I_n$	$\frac{\sin 2\omega_1}{2}$ (3) $I_0I_{2n}'+I_1I_{2n}$	$\frac{\sin 3\omega_1}{3}$ (4) $I_0I_{3n}'+I_1I_{3n}$	$\frac{\sin 4\omega_1}{4}$ (5) $I_0I_{4n}'+I_1I_{4n}$	$\frac{\sin 5\omega_1}{5}$ (6) $I_0I_{5n}'+I_1I_{5n}$	$\frac{\sin 6\omega_1}{6}$ (7) $I_0I_{6n}'+I_1I_{6n}$	$\frac{\sin 7\omega_1}{7}$ (8) $I_0I_{7n}'+I_1I_{7n}$	$\frac{\sin 8\omega_1}{8}$ (9) $I_0I_{8n}'+I_1I_{8n}$	$\frac{\sin 9\omega_1}{9}$ (10) $I_0I_{9n}'+I_1I_{9n}$	$(\pi-\omega_1)q^2I_1K_0$ $+\omega_1q^2I_0K_1$
(2)	$\omega_1-\frac{\pi}{2}+\frac{\sin 2\omega_1}{2}$ (11) I_nI_n'	$\frac{\sin\omega_1}{2}+\frac{\sin 3\omega_1}{6}$ (12) $I_nI_{2n}'+I_n'I_{2n}$	$\frac{\sin 2\omega_1}{4}+\frac{\sin 4\omega_1}{8}$ (13) $I_nI_{3n}'+I_n'I_{3n}$	$\frac{\sin 3\omega_1}{6}+\frac{\sin 5\omega_1}{10}$ (14) $I_nI_{4n}'+I_n'I_{4n}$	$\frac{\sin 4\omega_1}{8}+\frac{\sin 6\omega_1}{12}$ (15) $I_nI_{5n}'+I_n'I_{5n}$	$\frac{\sin 5\omega_1}{10}+\frac{\sin 7\omega_1}{14}$ (16) $I_nI_{6n}'+I_n'I_{6n}$	$\frac{\sin 6\omega_1}{12}+\frac{\sin 8\omega_1}{16}$ (17) $I_nI_{7n}'+I_n'I_{7n}$	$\frac{\sin 7\omega_1}{14}+\frac{\sin 9\omega_1}{18}$ (18) $I_nI_{8n}'+I_n'I_{8n}$	$\frac{\sin 8\omega_1}{16}+\frac{\sin 10\omega_1}{20}$ (19) $I_nI_{9n}'+I_n'I_{9n}$	$\sin\omega_1$ $-q^2(I_n'K_0-I_nK_1)$
(3)	(12)	$\omega_1-\frac{\pi}{2}+\frac{\sin 4\omega_1}{4}$ (20) $I_{2n}I_{2n}'$	$\frac{\sin\omega_1}{2}+\frac{\sin 5\omega_1}{10}$ (21) $I_{2n}I_{3n}'+I_{2n}'I_{3n}$	$\frac{\sin 2\omega_1}{4}+\frac{\sin 6\omega_1}{12}$ (22) $I_{2n}I_{4n}'+I_{2n}'I_{4n}$	$\frac{\sin 3\omega_1}{6}+\frac{\sin 7\omega_1}{14}$ (23) $I_{2n}I_{5n}'+I_{2n}'I_{5n}$	$\frac{\sin 4\omega_1}{8}+\frac{\sin 8\omega_1}{16}$ (24) $I_{2n}I_{6n}'+I_{2n}'I_{6n}$	$\frac{\sin 5\omega_1}{10}+\frac{\sin 9\omega_1}{18}$ (25) $I_{2n}I_{7n}'+I_{2n}'I_{7n}$	$\frac{\sin 6\omega_1}{12}+\frac{\sin 10\omega_1}{20}$ (26) $I_{2n}I_{8n}'+I_{2n}'I_{8n}$	$\frac{\sin 7\omega_1}{14}+\frac{\sin 11\omega_1}{22}$ (27) $I_{2n}I_{9n}'+I_{2n}'I_{9n}$	$\frac{\sin 2\omega_1}{2}$ $-q^2(I_{2n}'K_0-I_{2n}K_1)$
(4)	(13)	(21)	$\omega_1-\frac{\pi}{2}+\frac{\sin 6\omega_1}{6}$ (28) $I_{3n}I_{3n}'$	$\frac{\sin\omega_1}{2}+\frac{\sin 7\omega_1}{14}$ (29) $I_{3n}I_{4n}'+I_{3n}'I_{4n}$	$\frac{\sin 2\omega_1}{4}+\frac{\sin 8\omega_1}{16}$ (30) $I_{3n}I_{5n}'+I_{3n}'I_{5n}$	$\frac{\sin 3\omega_1}{6}+\frac{\sin 9\omega_1}{18}$ (31) $I_{3n}I_{6n}'+I_{3n}'I_{6n}$	$\frac{\sin 4\omega_1}{8}+\frac{\sin 10\omega_1}{20}$ (32) $I_{3n}I_{7n}'+I_{3n}'I_{7n}$	$\frac{\sin 5\omega_1}{10}+\frac{\sin 11\omega_1}{22}$ (33) $I_{3n}I_{8n}'+I_{3n}'I_{8n}$	$\frac{\sin 6\omega_1}{12}+\frac{\sin 12\omega_1}{24}$ (34) $I_{3n}I_{9n}'+I_{3n}'I_{9n}$	$\frac{\sin 3\omega_1}{3}$ $-q^2(I_{3n}'K_0-I_{3n}K_1)$
(5)	(14)	(22)	(29)	$\omega_1-\frac{\pi}{2}+\frac{\sin 8\omega_1}{8}$ (35) $I_{4n}I_{4n}'$	$\frac{\sin\omega_1}{2}+\frac{\sin 9\omega_1}{18}$ (36) $I_{4n}I_{5n}'+I_{4n}'I_{5n}$	$\frac{\sin 2\omega_1}{4}+\frac{\sin 10\omega_1}{20}$ (37) $I_{4n}I_{6n}'+I_{4n}'I_{6n}$	$\frac{\sin 3\omega_1}{6}+\frac{\sin 11\omega_1}{22}$ (38) $I_{4n}I_{7n}'+I_{4n}'I_{7n}$	$\frac{\sin 4\omega_1}{8}+\frac{\sin 12\omega_1}{24}$ (39) $I_{4n}I_{8n}'+I_{4n}'I_{8n}$	$\frac{\sin 5\omega_1}{10}+\frac{\sin 13\omega_1}{26}$ (40) $I_{4n}I_{9n}'+I_{4n}'I_{9n}$	$\frac{\sin 4\omega_1}{4}$ $-q^2(I_{4n}'K_0-I_{4n}K_1)$
(6)	(15)	(23)	(30)	(36)	$\omega_1-\frac{\pi}{2}+\frac{\sin 10\omega_1}{10}$ (41) $I_{5n}I_{5n}'$	$\frac{\sin\omega_1}{2}+\frac{\sin 11\omega_1}{22}$ (42) $I_{5n}I_{6n}'+I_{5n}'I_{6n}$	$\frac{\sin 2\omega_1}{4}+\frac{\sin 12\omega_1}{24}$ (43) $I_{5n}I_{7n}'+I_{5n}'I_{7n}$	$\frac{\sin 3\omega_1}{6}+\frac{\sin 13\omega_1}{26}$ (44) $I_{5n}I_{8n}'+I_{5n}'I_{8n}$	$\frac{\sin 4\omega_1}{8}+\frac{\sin 14\omega_1}{28}$ (45) $I_{5n}I_{9n}'+I_{5n}'I_{9n}$	$\frac{\sin 5\omega_1}{5}$ $-q^2(I_{5n}'K_0-I_{5n}K_1)$
(7)	(16)	(24)	(31)	(37)	(42)	$\omega_1-\frac{\pi}{2}+\frac{\sin 12\omega_1}{12}$ (46) $I_{6n}I_{6n}'$	$\frac{\sin\omega_1}{2}+\frac{\sin 13\omega_1}{26}$ (47) $I_{6n}I_{7n}'+I_{6n}'I_{7n}$	$\frac{\sin 2\omega_1}{4}+\frac{\sin 14\omega_1}{28}$ (48) $I_{6n}I_{8n}'+I_{6n}'I_{8n}$	$\frac{\sin 3\omega_1}{6}+\frac{\sin 15\omega_1}{30}$ (49) $I_{6n}I_{9n}'+I_{6n}'I_{9n}$	$\frac{\sin 6\omega_1}{6}$ $-q^2(I_{6n}'K_0-I_{6n}K_1)$
(8)	(17)	(25)	(32)	(38)	(43)	(47)	$\omega_1-\frac{\pi}{2}+\frac{\sin 14\omega_1}{14}$ (50) $I_{7n}I_{7n}'$	$\frac{\sin\omega_1}{2}+\frac{\sin 15\omega_1}{30}$ (51) $I_{7n}I_{8n}'+I_{7n}'I_{8n}$	$\frac{\sin 2\omega_1}{4}+\frac{\sin 16\omega_1}{32}$ (52) $I_{7n}I_{9n}'+I_{7n}'I_{9n}$	$\frac{\sin 7\omega_1}{7}$ $-q^2(I_{7n}'K_0-I_{7n}K_1)$
(9)	(18)	(26)	(33)	(39)	(44)	(48)	(51)	$\omega_1-\frac{\pi}{2}+\frac{\sin 16\omega_1}{16}$ (53) $I_{8n}I_{8n}'$	$\frac{\sin\omega_1}{2}+\frac{\sin 17\omega_1}{34}$ (54) $I_{8n}I_{9n}'+I_{8n}'I_{9n}$	$\frac{\sin 8\omega_1}{8}$ $-q^2(I_{8n}'K_0-I_{8n}K_1)$
(10)	(19)	(27)	(34)	(40)	(45)	(49)	(52)	(54)	$\omega_1-\frac{\pi}{2}+\frac{\sin 18\omega_1}{18}$ (55) $I_{9n}I_{9n}'$	$\frac{\sin 9\omega_1}{9}$ $-q^2(I_{9n}'K_0-I_{9n}K_1)$

(43) were divergent. It is reasonable to suppose, however, that the interference near the center is largely determined by average conditions at the boundary rather than by the detailed boundary conditions, and these average conditions could be expressed by means of a Fourier series. In any case, the potential only a short distance from the boundary could certainly be expressed in Fourier series. The problem at hand, therefore, is the determination to a sufficient degree of approximation of the first few functions P_0, P_1, P_2, P_3, ...

As a first attempt to obtain numerical solutions, four of the simultaneous equations (43) with the first four functions P_0 . . . P_3 were solved at various values of q for $n=10$ (10 slots) and values of ω_1 of 0.5π, 0.6π, 0.75π, and 0.875π. The axial interference velocities at the position of the doublet ($\rho=\xi=0$) according to equation (45) are shown by the circled points in figure 3, where they may be compared with the corresponding values for the open and closed tunnels. It was realized that the number of equations used in the solution was entirely inadequate for obtaining accurate values of the interference, but since the interference at the center must depend largely on the mean boundary conditions, it was thought that some indication of the slot effect could be obtained. The nonuniformity of convergence of the Fourier series is such, however, that with the smaller slot widths, since in these cases the edge of the slot dominates the whole slot region, even the mean boundary conditions would not be adequately expressed, and an attempt to calculate the interference with $\omega_1=0.95\pi$ ended in failure because the integrand in the infinite integral of equation (45) became positively and negatively infinite at a point within the range of integration. The course of the calculated values (fig. 3) and the behavior of the calculations were such, however, that it was surmised that the interference at the position of

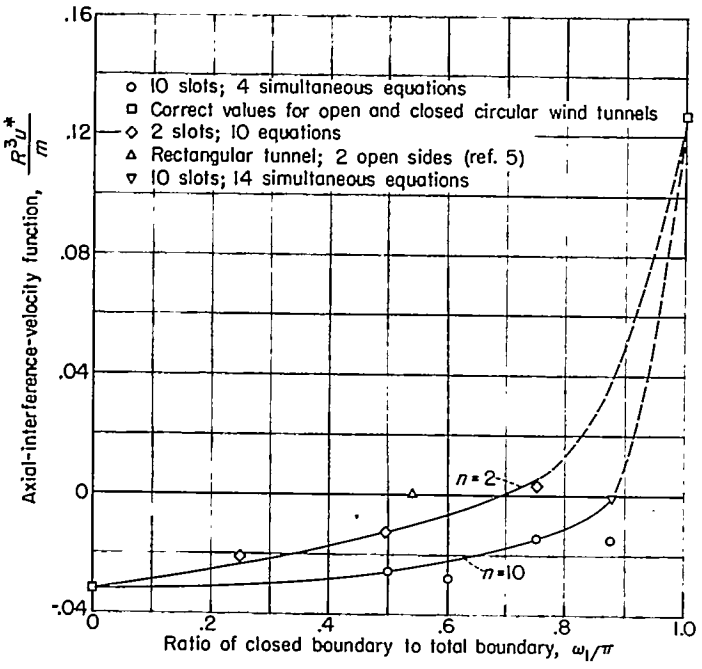

FIGURE 3.—Axial-interference-velocity function in slotted tunnels. $\rho=\xi=0$.

the doublet should become zero for a value of ω_1 near 0.875π. On the basis of these meager results, an experimental investigation was planned.

The 10 by 10 system of table I (with some allowable modification in order to keep the numbers involved within the range of the computing machine) was next solved on the Bell Telephone Laboratories X–66744 relay computer for $n=2$ and values of ω_1 of 0.25π, 0.75π, and 0.49π, the last value being chosen instead of 0.5π because the Bell machine was not set to carry the zero coefficients that would appear in many of the squares for $\omega_1=0.5\pi$. The values obtained for the interference velocity at the position of the doublet are shown by the diamonds in figure 3. The value $n=2$ was chosen because it was believed that with $n=2$ the value of ω_1, for zero interference, would be of a lower value, for which the problem of convergence would be less severe, and it was desired to investigate the satisfaction of the boundary conditions in this region under the most favorable computing conditions. Also, a comparison was desired between the interference for the two-slot circular tunnel and the interference for the rectangular tunnel with two free sides which was discussed in reference 5. The fact that the interference-velocity value for the rectangular tunnel with two open sides (shown by the upright triangle in fig. 3) falls above the values calculated for the two-slot circular tunnel does not indicate that these values are incorrect, because the more strongly effective central part of the closed surface lies closer to the doublet position in the rectangular tunnel than in the circular tunnel, and the interference-velocity value might therefore be expected to lie nearer to the closed-tunnel value.

The interference at the doublet position with $n=10$ and $\omega_1=0.875\pi$ has recently been calculated on the Bell Telephone Laboratories X–66744 relay computer with 14 equations of the system (43). The results shown in figure 3 verify the assumption previously made that for this configuration the interference would be approximately zero.

With regard to compressibility effects, the method described in the appendix of reference 6 is applicable. By this method, the whole system is stretched in the flow direction by the ratio $\frac{1}{\sqrt{1-M^2}}$, where M is the free-stream Mach number. In this process, the tunnel boundary remains unchanged since in the theory it already extends uniformly to infinity. Because of the stretching of the body, however, the strength of the doublet used to represent it must be increased approximately in the ratio $\frac{1}{\sqrt{1-M^2}}$. Since, according to reference 6, the velocities induced in the compressible flow are increased in the ratio $\frac{1}{1-M^2}$ in the stream direction and $\frac{1}{\sqrt{1-M^2}}$ normal to the stream direction over the incompressible induced velocities for the stretched system and since the tunnel-wall interference velocities are proportional to the doublet strength, the effect of compressibility is to increase the axial interference velocities in the ratio $\frac{1}{(1-M^2)^{3/2}}$ and the interference velocities normal to the axis in the ratio $\frac{1}{1-M^2}$. It therefore follows that if the interference is zero for the incompressible flow it is also zero for compressible flow. This reasoning is valid, moreover, even though the critical speed of the body be exceeded, because the presence of supersonic regions about the model could be taken into account merely by increasing the doublet strength still further; the nature of the tunnel-wall constriction effect remains unchanged. Any distortion present, that is, increase in interference velocities away from the doublet position, would be magnified by compressibility and might become too large to be tolerated as Mach number unity is approached. It therefore appears that, as is true with conventional wind tunnels, the size of the model must be decreased as the Mach number is increased. At any given Mach number, however, it should be possible to test much larger models in a slotted tunnel of a given size than could be tested in a closed tunnel of the same size.

Once the supersonic region has reached the tunnel wall, the theory herein presented is no longer valid. A consideration of the nature of wind-tunnel choking indicates, however, that choking need not occur, because the excess mass flow can bypass the model by flowing out through the slots into the tank ahead of the model and can enter again through the slots behind the model.

As may be seen from figure 3, for slot widths greater than that just sufficient to secure zero interference at the center the operation of the slotted tunnel is relatively insensitive to slot width. This characteristic provides some possibility of compromise with regard to varying the slot width in order to reduce the lift interference, which has not yet been investigated, and with regard to possible supersonic operation. Otherwise, it seems desirable to keep the slot width as small as practicable in order to minimize the power requirement. In this regard, it may be inferred from figure 3 that the

greater the number of slots the smaller is the ratio of open periphery to closed periphery required to attain the zero-interference condition. The power required for a slotted tunnel should be much less than that needed for an open tunnel.

EXPERIMENTAL INVESTIGATION

SYMBOLS

The following symbols are used in presenting the results of the experimental investigation:

a	velocity of sound in air
b	wing span
c	wing chord
D	diameter of tunnel at throat
D'	effective diameter of octagonal tunnel
H	total pressure
l	body length
M	free-stream Mach number (V/a)
M_0	free-stream Mach number at midpoint of test section
M_F	free-stream Mach number at position of body nose
M_R	free-stream Mach number at position of body tail
p	absolute static pressure
$(p/H)_{cr}$	critical pressure ratio (M=1.0)
R	test section radius of circular tunnel
R'	effective radius of octagonal test section
S	distance from midpoint of test section along tunnel longitudinal axis
V	free-stream velocity
x_b	distance along body axis from nose
x_w	distance along wing chord from leading edge
y	distance along wing span from plane of symmetry

TESTS WITH 3.5-INCH-DIAMETER BODY

Apparatus and methods.—Preliminary tests in this investigation were conducted in a 12-inch-diameter circular test section slotted in the direction of flow. This test section was designed on the basis of the preceding theory to produce zero blockage interference at the position of the model. Ten evenly spaced longitudinal slots comprised one-eighth of the total circular periphery. The slot width remained constant along its length and extended downstream to a station in the diffuser where the area was 20 percent greater than that at the throat area. At this station the effuser bell became tangent to the diffuser. A closed tank 24 inches in diameter surrounded the test section. A longitudinal schematic diagram of the slotted test section and a scaled cross-sectional view of the circular slotted test section are included in figure 4. Some of the important slotted test-section parameters are included in table II.

The test model was a 3.5-inch-diameter prolate spheroid of fineness ratio 6 (table III). The ratio of body diameter to tunnel diameter is 0.292. The selection of a body of such large size was made in order to magnify the wall-interference effect to permit an accurate treatment of the wall-interference effects. Static-pressure orifices were installed in the body along top and bottom meridians and at several angular stations about the center of the body.

TABLE II

TRANSONIC-SLOTTED-TEST-SECTION PARAMETERS

[See fig. 4]

Item	Circular	Octagonal
Diameter (in.)	12	12 (effective).
Length-diameter ratio	3	1.5.
Number of slots	10	8.
Ratio of sum of slot widths to total periphery.	1:8	1:8.
Included angle of longitudinal slot divergence (deg.).	0	0.1.
Included angle of radial slot divergence (deg.).	90	45.
Wall divergence from minimum throat area (in./in.).	0.005	0.002.
Area increase over minimum where effuser bell becomes tangent to diffuser (percent).	20 (approx.)	20 (approx.).
Effuser bell	Long	Short.
Ratio of tank diameter to test-section diameter.	2	1.5.

The local static pressures over the body were recorded simultaneously with the free-stream Mach number in all tunnel configurations.

In order to obtain for comparison an experimental "free-air" or essentially interference-free condition for the model, tests were also performed on the same model in the Langley 8-foot high-speed tunnel. For further comparison, tests were made in 12-inch-diameter open and closed test sections, and the results were corrected by means of a potential-flow method. The data from the 8-foot-diameter closed tunnel were essentially free of interference as recorded.

Results and discussion.—Surveys of the pressure distributions at the center and at the wall of the slotted test section indicated a satisfactorily uniform test region at all subsonic Mach numbers. (See fig. 5.) Supersonic Mach numbers were obtained merely by increasing the pressure drop across the

TABLE III

PROLATE-SPHEROID ORDINATES

x_b/l	3.5-inch-diameter body (fineness ratio 6)		1.333-inch-diameter body (fineness ratio 6)	
	Station (in.)	Radius (in.)	Station (in.)	Radius (in.)
0	0		0	0
.0025	.0525	.1750	.0200	.0667
.0075	.1575	.3016	.0600	.1149
.0100	.2100	.3483	.0800	.1327
.0125	.2625	.3896	.1000	.1484
.0250	.5250	.5464	.2000	.2082
.0500	1.0500	.7628	.4000	.2906
.1000	2.1000	1.0500	.8000	.4000
.1500	3.1500	1.2497	1.2000	.4761
.2000	4.2000	1.4000	1.6000	.5333
.2500	5.2500	1.5159	2.0000	.5775
.3000	6.3000	1.6040	2.4000	.6110
.3500	7.3500	1.6694	2.8000	.6360
.4000	8.4000	1.7147	3.2000	.6532
.4548	9.5500	1.7413	3.6380	.6634
.4834	10.1500	1.7478	3.8670	.6658
.5000	10.5000	1.7500	4.0000	.6667
.5166	10.8500	1.7478	4.1330	.6658
.5453	11.4500	1.7413	4.3620	.6634
.6000	12.6000	1.7147	4.8000	.6532
.6500	13.6500	1.6694	5.2000	.6360
.7000	14.7000	1.6040	5.6000	.6110
.7500	15.7500	1.5159	6.0000	.5775
.8000	16.8000	1.4000	6.4000	.5333
.8500	17.8500	1.2497	6.8000	.4761
.9000	18.9000	1.0500	7.2000	.4000
.9286	19.5000	.9450	7.4290	.3600
.9584	20.1250	.8340	7.6670	.3177
1.0000	21.0000	.6795	8.0000	.2589

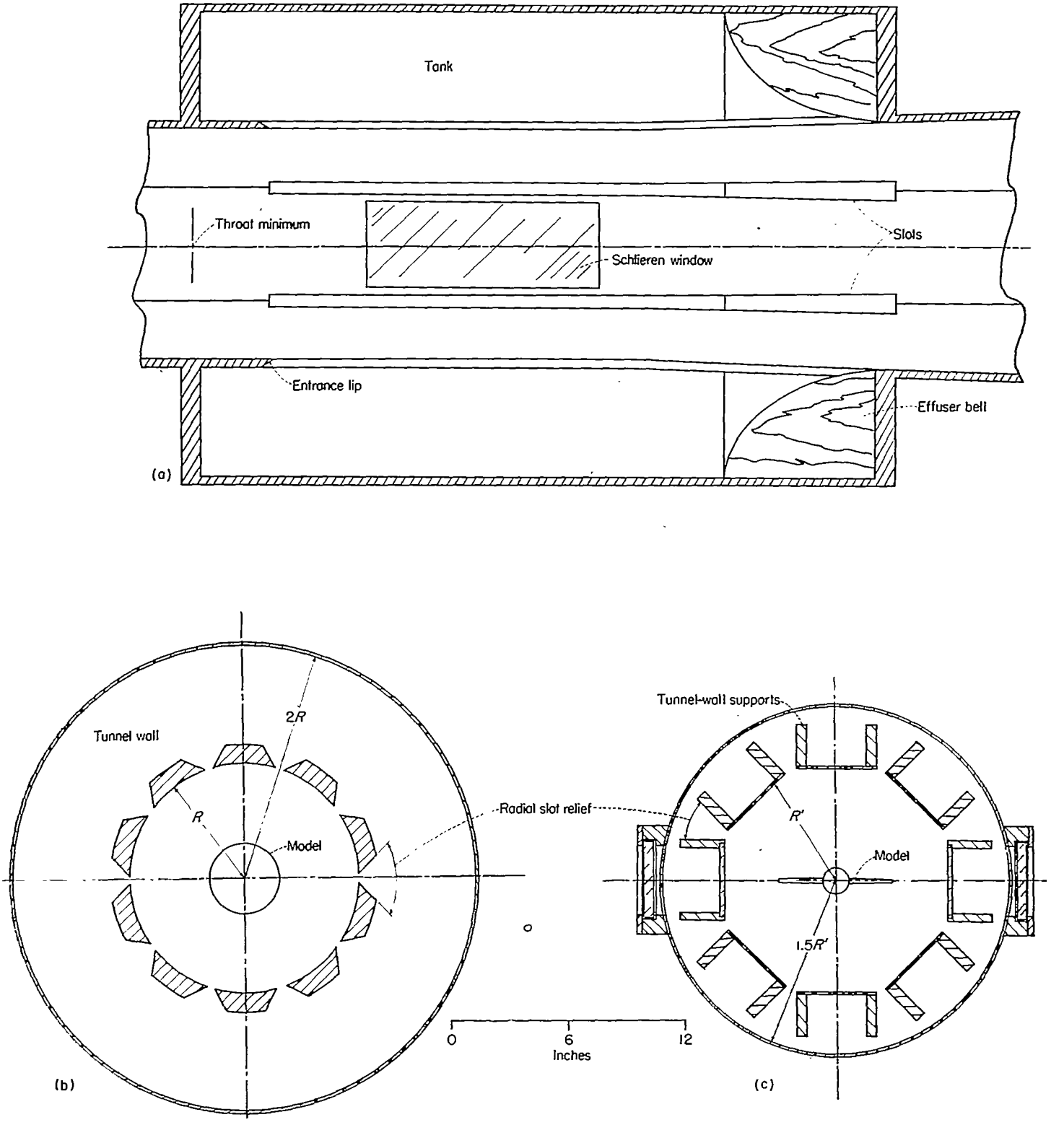

(a) Schematic diagram of transonic slotted tunnel.
(b) Cross section of 12-inch-diameter circular transonic slotted tunnel.
(c) Cross section of 12-inch-effective-diameter octagonal transonic slotted tunnel.

FIGURE 4.—Transonic-slotted-tunnel configurations.

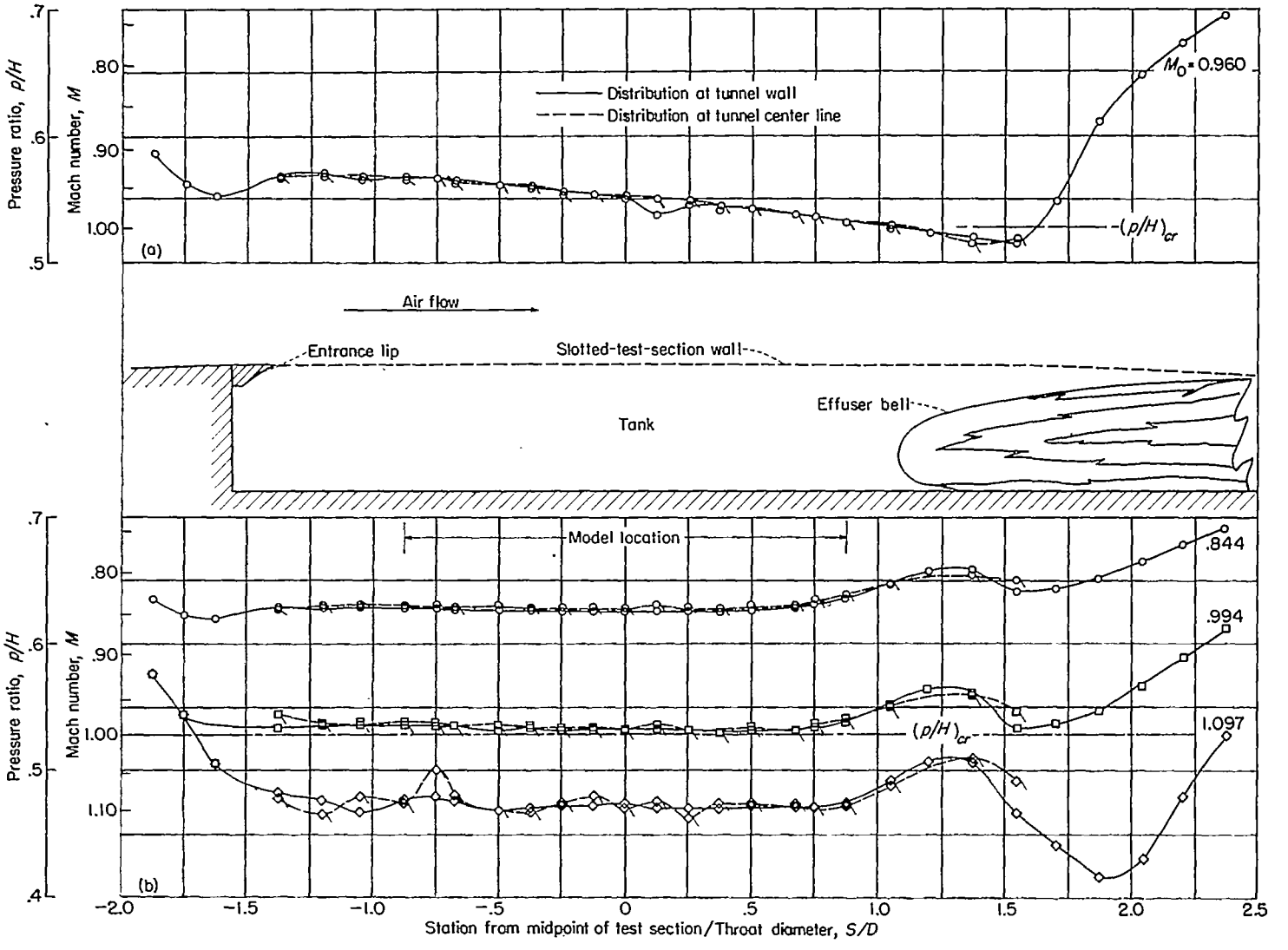

(a) 12-inch-diameter circular closed tunnel.
(b) 12-inch-diameter circular transonic slotted tunnel.

FIGURE 5.—Axial pressure distributions along wall and center line of circular closed and slotted tunnels for several Mach numbers. (Flagged symbols are for distributions at center line.)

test section. With a supersonic Mach number of 1.097, the Mach number variations appeared to be ±0.02 over a length of one throat diameter. Center-line pressures were obtained by means of a ⅜-inch-diameter axial static-pressure survey tube that extended upstream to the tunnel entrance bell. The axial pressure distribution at an indicated stream Mach number of 0.960 in the 12-inch-diameter closed tunnel is included in this figure for comparison. Small axial pressure gradients existed in the 12-inch-diameter open and closed tunnels and at the highest subsonic Mach numbers in the 8-foot-diameter closed tunnel. The Mach number calibrations for all tunnels were based on pressures at orifices located in the closed entrance section upstream of the throat.

With the 3.5-inch-diameter body in the 12-inch-diameter closed test section, the Mach number was limited to 0.72 by choking at the model, whereas in the open test section choking at the effuser bell limited the maximum test Mach number to 0.89. In the slotted test section choking again occurred at the effuser bell, but since the mixing region w now limited only to the slots and the low-energy air at th boundary was therefore less than that produced in th open tunnel, a maximum Mach number of 0.97 could b obtained. In the 8-foot closed test section a maximum tes Mach number of 0.94 was obtained rather than the valu 0.96 indicated by theoretical one-dimensional choking a the model. The 8-foot tunnel is therefore believed to hav choked at the support strut behind the model.

The measured local pressure ratios at the midpoint of th 3.5-inch-diameter prolate spheroid in the 12-inch-diamete and 8-foot-diameter tunnel configurations corrected for th small pressure gradients that existed in the closed-throa tunnels are presented as a function of Mach number figure 6. Even with this large model in the 12-inch-diamete slotted tunnel, the pressure ratios show reasonably goo agreement over almost the entire test Mach number rang with values obtained in the 8-foot-diameter closed tunne This behavior is in sharp contrast with that in the 12-inc

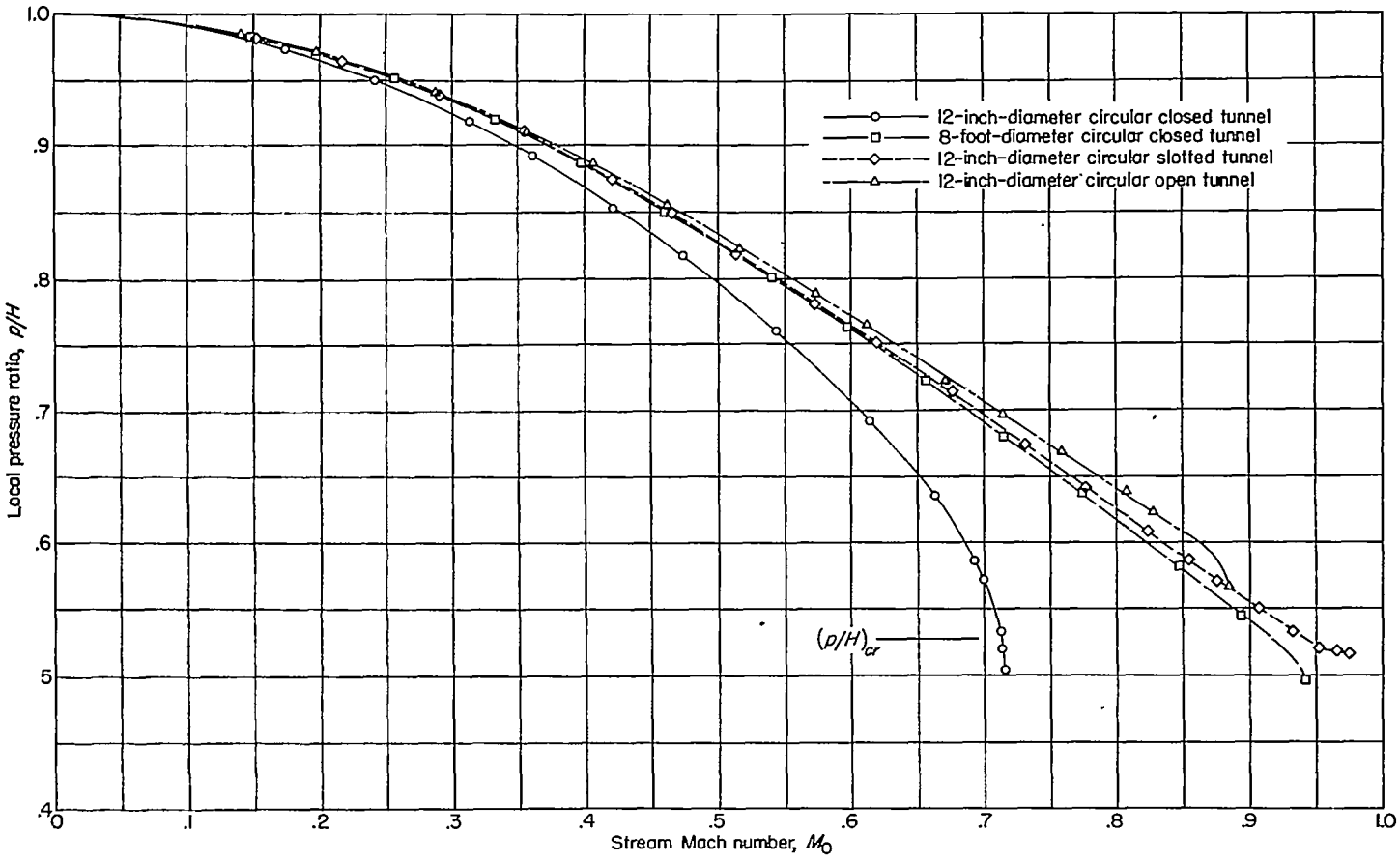

FIGURE 6.—Comparison of local pressure as a function of Mach number at midpoint of 3.5-inch-diameter prolate spheroid in circular open, closed, and slotted tunnels.

diameter closed tunnel, for which the blockage interference is very large. A large high subsonic Mach number range is covered in the 12-inch-diameter slotted tunnel which cannot be reached in the 12-inch-diameter closed tunnel because of choking at the model.

Figure 7 presents the measured local pressure ratios p/H in the slotted tunnel compared with the pressure ratios obtained from the corrected data from the 8-foot-diameter closed tunnel and from the 12-inch-diameter open and closed tunnels. The curve from the slotted test section falls between the two zero-interference curves and extends to high subsonic Mach numbers for which adequate correction for the interference cannot be made.

The pressure distributions over the 3.5-inch-diameter prolate spheroid are compared at several Mach numbers with the two zero interference curves in figure 8. The pressure distribution obtained from the linearized potential theory is also shown. A rotation of the pressure diagram in the slotted test section is evident in the sense of increasing pressures toward the nose of the body. The pressure-ratio scale has been doubled relative to that in previous figures in order to define more clearly this distortion. It is believed that this distortion of the pressure distribution is due to the inordinately large model used in these preliminary experiments. Even so, it is also believed that the distortion might be corrected by tapering the slot widths. Study of this phase of the problem has been deferred, however, in order to proceed to the more important investigation of the transonic behavior of this type of test section with models of more reasonable size.

TESTS WITH 1.333-INCH-DIAMETER MODEL

Apparatus and methods.—The second model used in this investigation consisted of a 1.333-inch-diameter prolate spheroid, of fineness ratio 6, fitted with an NACA 65–010 wing of 1.5-inch chord and 6-inch span. (See tables III and IV.) The orifice locations on the model are presented in figure 9.

TABLE IV

ORDINATES OF NACA 65–010 AIRFOIL

Station (percent chord)	Ordinate (percent chord)	Station (percent chord)	Ordinate (percent chord)
0	0	40.00	4.99
.50	.77	45.00	4.96
.75	.93	50.00	4.81
1.25	1.17	55.00	4.53
2.50	1.57	60.00	4.15
5.00	2.18	65.00	3.68
7.50	2.65	70.00	3.15
10.00	3.04	75.00	2.59
15.00	3.67	80.00	1.99
20.00	4.14	85.00	1.39
25.00	4.50	90.00	.81
30.00	4.76	95.00	.31
35.00	4.93	100.00	0

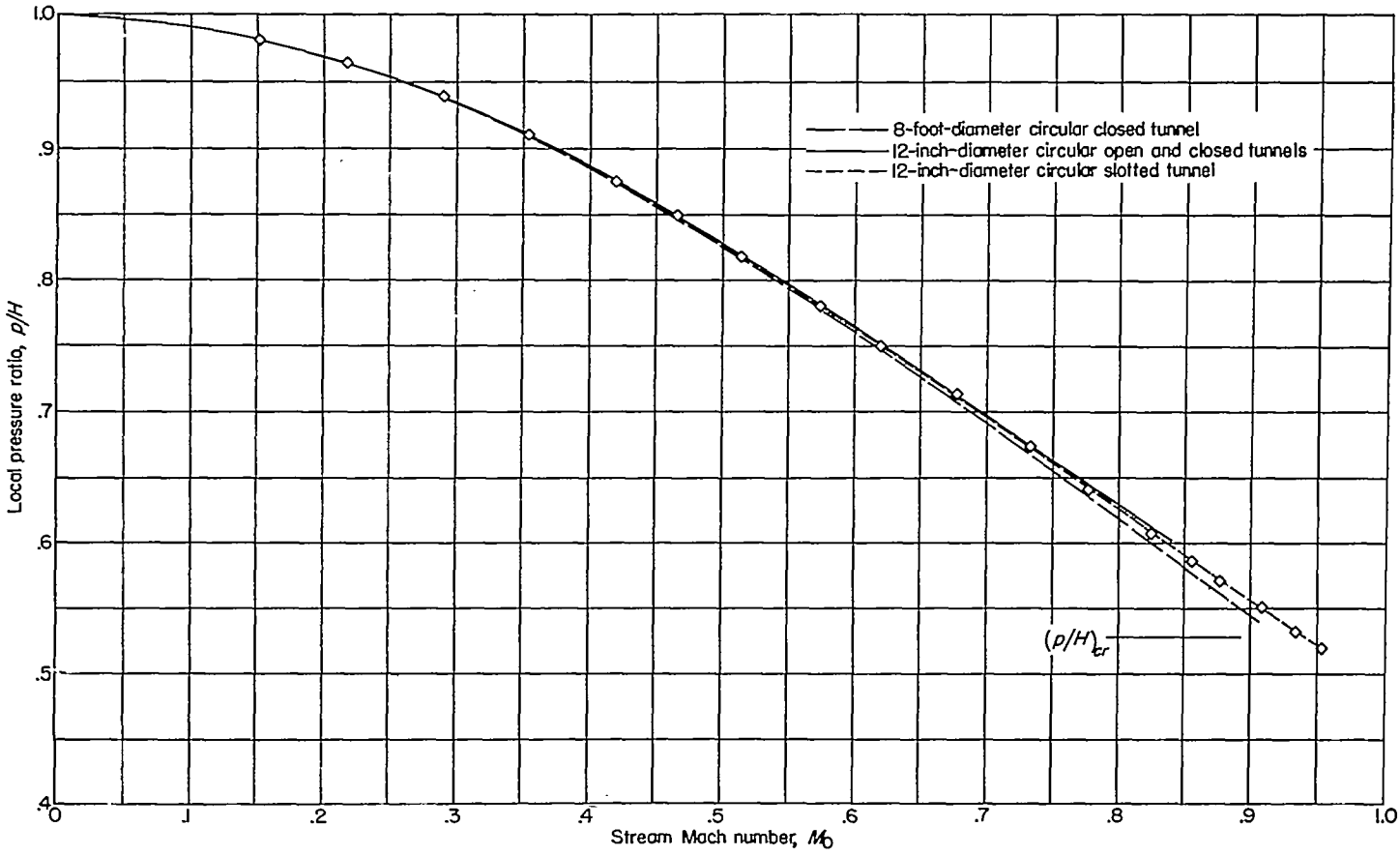

FIGURE 7.—Corrected local pressure ratio as a function of Mach number at position of midpoint of 3.5-inch-diameter prolate spheroid in circular open and closed tunnels compared with uncorrected local pressure ratio on body in circular slotted tunnel.

An octagonal slotted test section was substituted for the circular section used in the preliminary tests. Eight axial slots comprising one-eighth of the total periphery were located at the corners between the flat sides. (See fig. 4.) The length of the octagonal slotted test section was one-half the length of the circular slotted test section. The choice of the octagonal section was made as a result of studies of the application of this type of throat to large wind tunnels, specifically, the Langley 16-foot and 8-foot high-speed tunnels. Factors affecting the choice of test-section shape are installation of optical apparatus, simplicity of construction, and cost.

A calibration based on the measured tank pressure ahead of the slotted region was used to give Mach number variation both in the subsonic and in the supersonic region. The stream Mach number, calibrated in this manner, is used in the octagonal transonic slotted tunnel tests. Because of the existing supersonic Mach number gradients, all Mach numbers above the speed of sound are presented for the nose position of the test model M_F.

For comparison, data from the Langley 8-foot high-speed tunnel were utilized as the zero-interference condition. The 8-foot-diameter closed tunnel was limited to a subsonic Mach number of 0.99 by choking at or near the model. The interference effects on the model at all subsonic Mach numbers were found to be negligible. (See ref. 7.) One test point with zero Mach number gradient was obtained at Mach number 1.20. By moving the test model upstream in the supersonic nozzle of the 8-foot tunnel, additional test points at lower supersonic Mach numbers could be obtained with a positive Mach number gradient of about 0.03 from the nose to the tail of the body. As these test points were the best available for this Mach number range, and as the Mach number gradient was relatively small, the results in the 8-foot closed tunnel were treated as continuous data for these comparisons. Unless otherwise indicated, the Mach numbers specified for these data are those existing at the nose position of the model.

Results and discussion.—The axial pressure distributions along the center line and wall of the 12-inch-effective-diameter octagonal transonic slotted test section are presented in figure 10. The fact that higher supersonic Mach numbers were obtained in the octagonal slotted test section than in the circular test section is believed to be due to the shorter length of test section, since with this shorter length less low-energy air is required to pass into the diffuser. The Mach number variation near Mach number 1.27 is approximately ± 0.05 and decreases as the stream Mach number is reduced. At all subsonic Mach numbers, the Mach number in the test region is satisfactorily uniform.

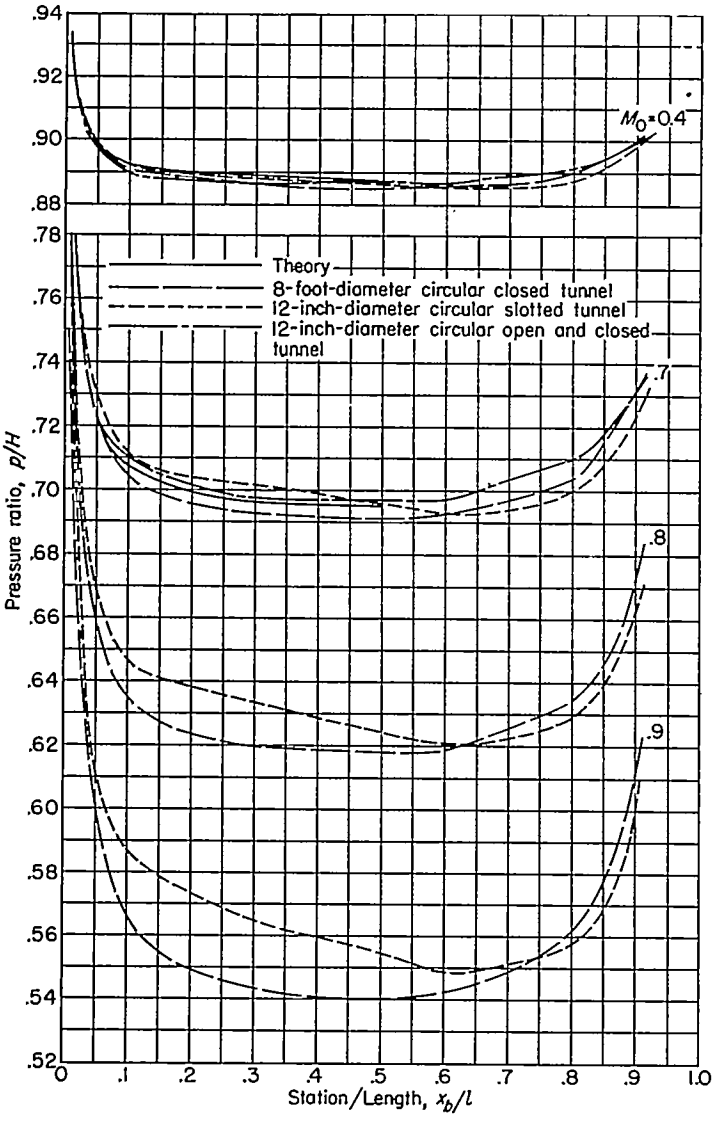

FIGURE 8.—Corrected pressure distributions along top meridian of 3.5-inch-diameter prolate spheroid for several Mach numbers in circular open and closed tunnels compared with uncorrected pressure distributions along body in circular slotted tunnel. (Note that scale of p/H is double that used in figs. 6 and 7.)

A point-by-point comparison of the local pressures over the 1.333-inch-diameter body in the 12-inch-diameter transonic slotted tunnel with those in the 8-foot-diameter closed tunnel are presented as a function of Mach number in figure 11. The pressures over most of the body appear to agree quite satisfactorily in the two tunnel configurations, even in the Mach number range between 0.88 and 1.13, for which this body cannot be tested, because of choking, in a closed tunnel of the same size as that of the slotted tunnel. Above a Mach number of 1.08 in the slotted tunnel, disagreement exists over a forward portion of the body in the nature of a pressure rise relative to the pressure variations obtained in the 8-foot-diameter closed tunnel. This pressure rise does not correlate with the nonuniformities in the tunnel-empty Mach number distributions. Neither do these nonuniformities appear to affect substantially the pressure distributions over the model. At x_b/l=0.90, the pressure differences between the data in the two tunnel configurations are larger than at the forward stations and appear to indicate a difference in the rate of shock movement with Mach number. Examination of reference 8 indicates that this effect may be due to the 25-percent greater Reynolds number and to the higher turbulence level in the 12-inch-diameter slotted tunnel as compared to the 8-foot-diameter closed tunnel. The nature of the pressure difference is such as to indicate this possibility. The Mach number gradient in the 8-foot tunnel for the low supersonic values tends also to show these points at a Mach number lower than actually exists, thereby exaggerating the aforementioned difference. The lower-surface and radial-station pressure variations are also presented in figure 11.

Figure 12 presents comparisons similar to those in figure 11 on the 1.333-inch-diameter prolate spheroid when the NACA 65–010 wing is affixed symmetrically to the body. A pressure

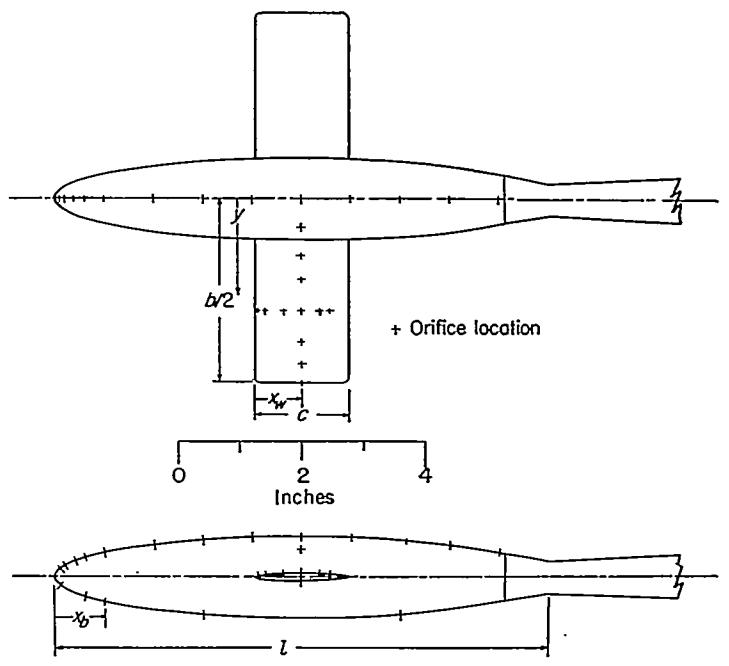

Orifice locations							
Body				Wing			
Surface	x_b/l at center line	Surface	x_b/l at center line	Surface	$\frac{y}{b/2}$ at 0.50c	Surface	x_w/c at $0.61b/2$
Upper	0.01 .02 .04 .06 .10 .20 .30 .40 .50 .60	Upper	0.70 .80 .90	Upper	0.157 .319 .443 .776 .901	Upper	0.025 .10 .30 .50 .70 .80
		Lower	.01 .06 .10 .30 .70	Tip	1.000		
		45° radial station	.50	Lower	.776 .901		

FIGURE 9.—Prolate spheroid of 1.333-inch diameter with NACA 65–010 wing affixed symmetrically.

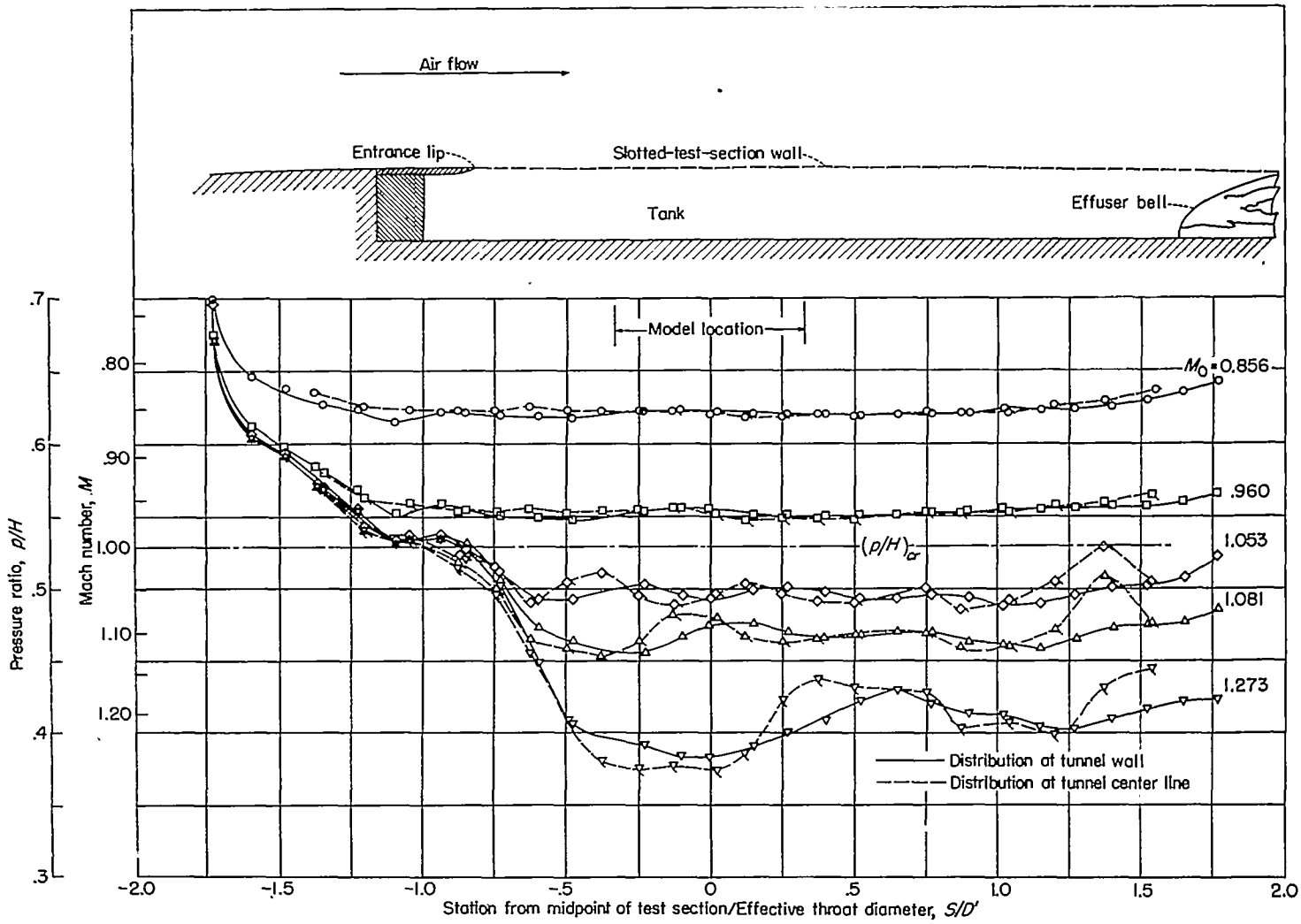

FIGURE 10.—Axial pressure distribution along wall and center line of 12-inch-effective-diameter octagonal transonic slotted tunnel for several Mach numbers.

rise over the forward portion of the body above a Mach number of 1.08 is again noted in the transonic slotted tunnel. Because of the large number of individual test runs necessary to obtain the supersonic test points in the 8-foot-diameter closed tunnel, the data presented for this configuration are limited to two points in the gradient flow between a Mach number of 1.0 and 1.2. The accuracy of the comparison in this Mach number range is therefore severely limited. Again the main disagreements between the data in the two tunnel configurations occur at the rear of the body, but the differences are smaller than with the body alone, a circumstance which supports the possibility that the differences may be due in part to Reynolds number and turbulence effects.

The local pressures over the NACA 65–010 wing are compared for the two tunnel configurations in figures 13 and 14. Figure 13 presents variations with Mach number at several stations along the chord. Figure 14 presents similar variations at spanwise positions. The main differences between the data in the two tunnel configurations again occur at the rearward chordwise stations. The disagreement is most severe above the critical speed of the wing but below a Mach number of unity. Again these effects may be due in part to Reynolds number and turbulence differences. The spanwise comparisons (fig. 14) appear to agree satisfactorily even at the wing-tip position, $\frac{y}{b/2}=1.000$.

The data are presented as pressure distributions in figures 15 to 18. The distributions on the body alone are shown for several Mach numbers in figure 15. The disagreement previously discussed may be noted in these distributions. The relative pressure rise that occurs in the slotted tunnel over the forward portion of the body is illustrated at Mach number 1.120. At $x_b/l=0.90$ the pressure differences obtained in the two tunnel configurations are evident for supersonic Mach numbers from 1.020 to 1.078.

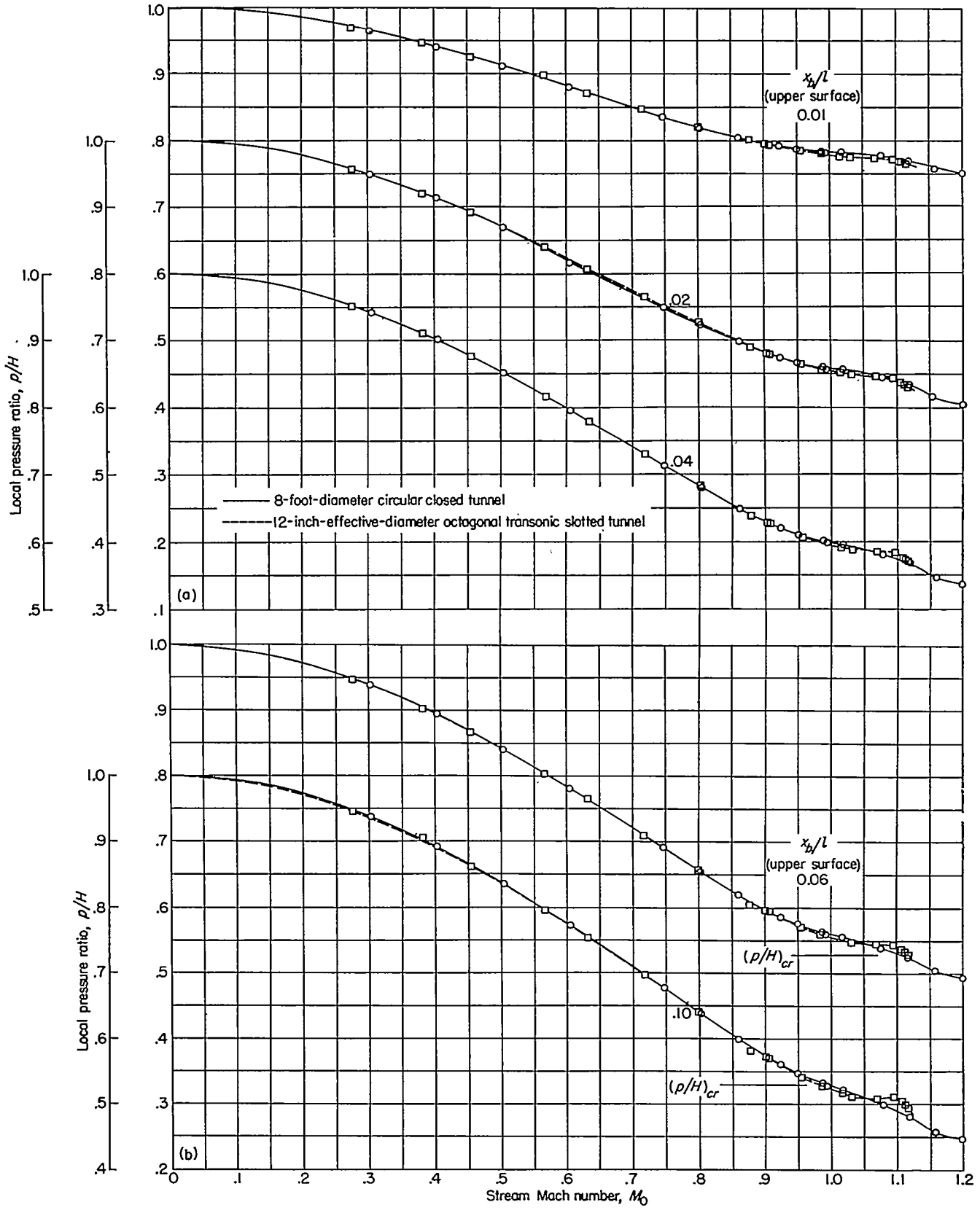

FIGURE 11.—Comparison of local pressures as a function of Mach number for several longitudinal stations along 1.333-inch-diameter prolate spheroid in the transonic slotted tunnel and in a large closed tunnel.

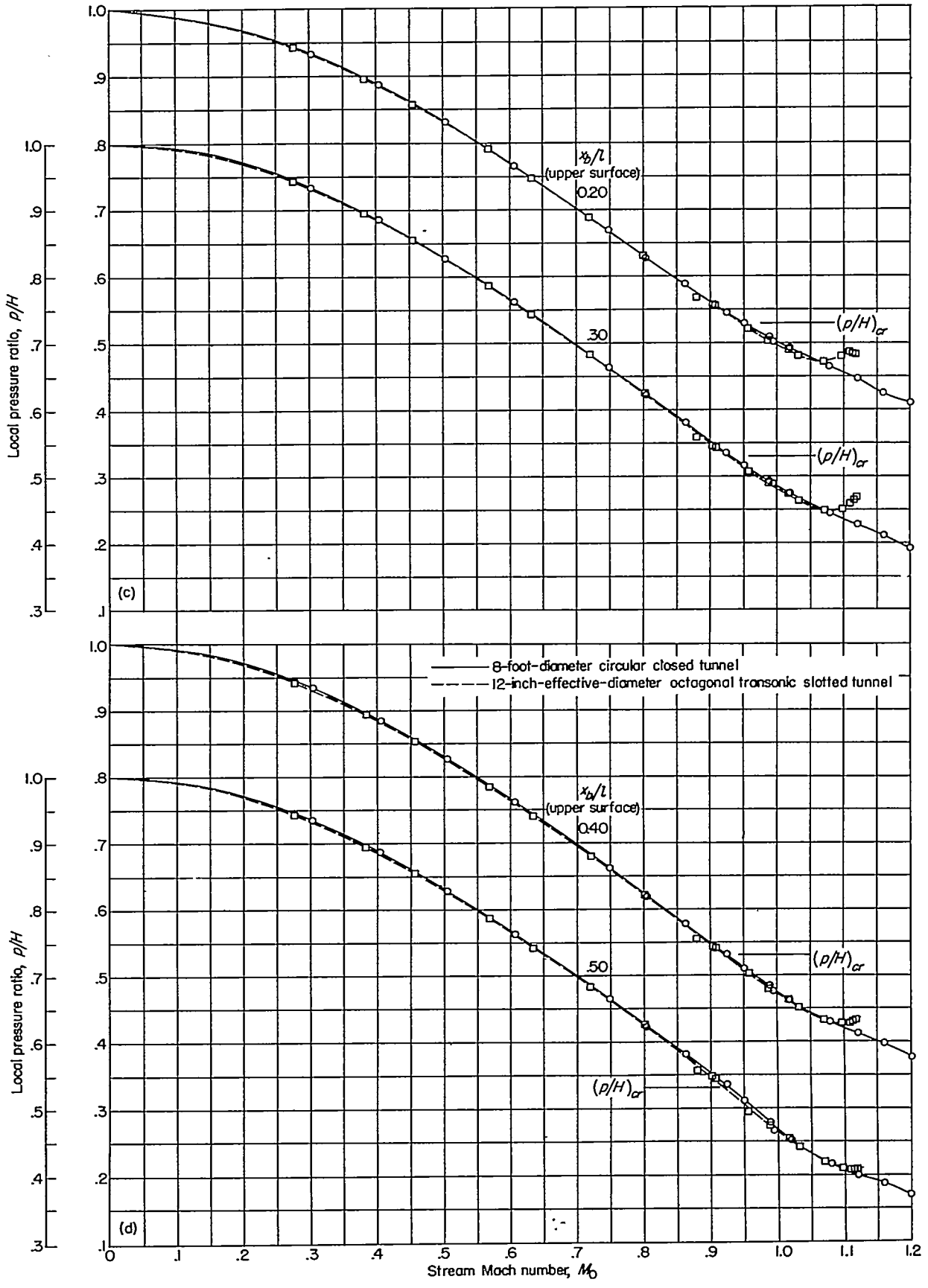

FIGURE 11.—Continued.

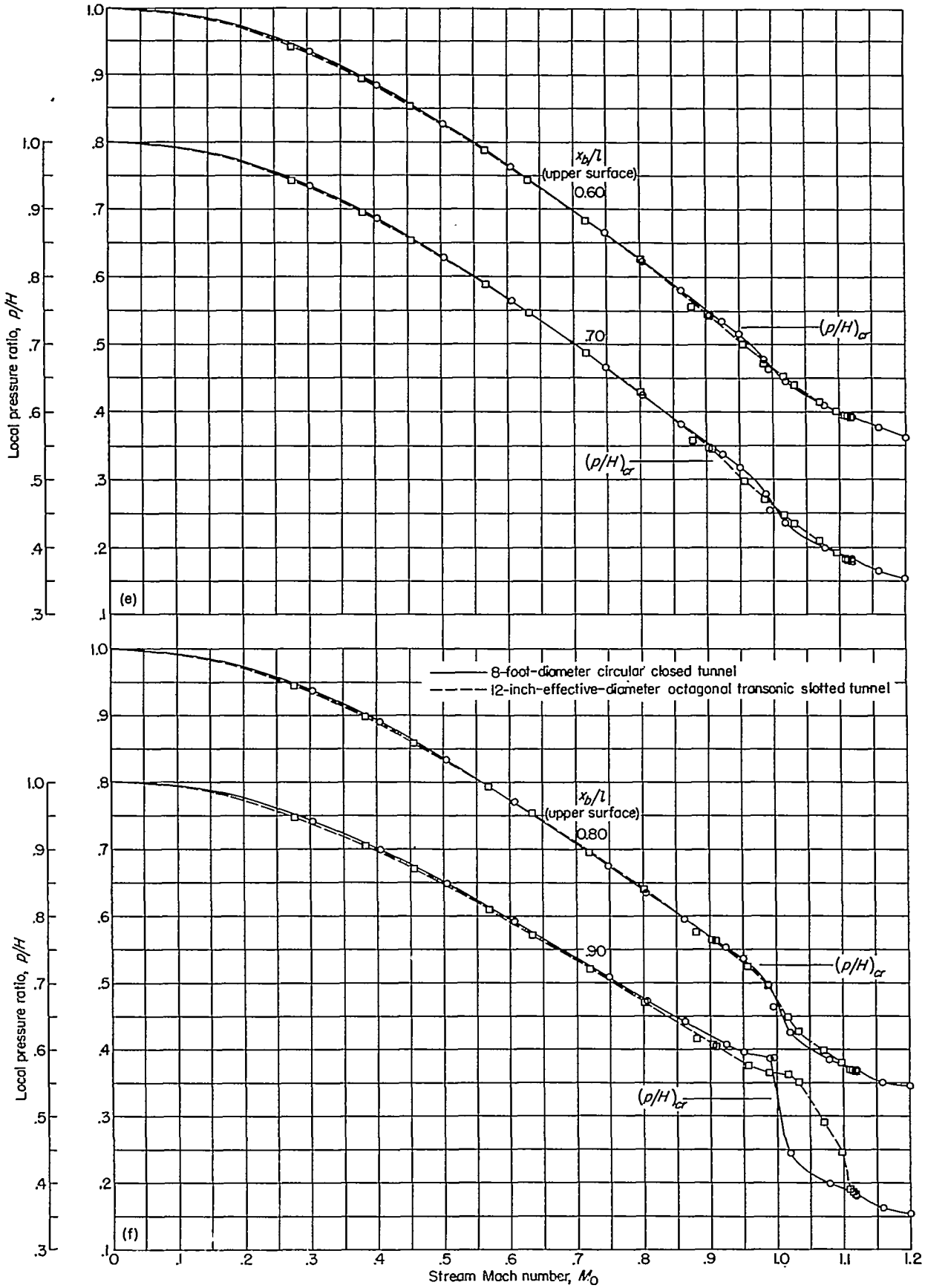

FIGURE 11.—Continued.

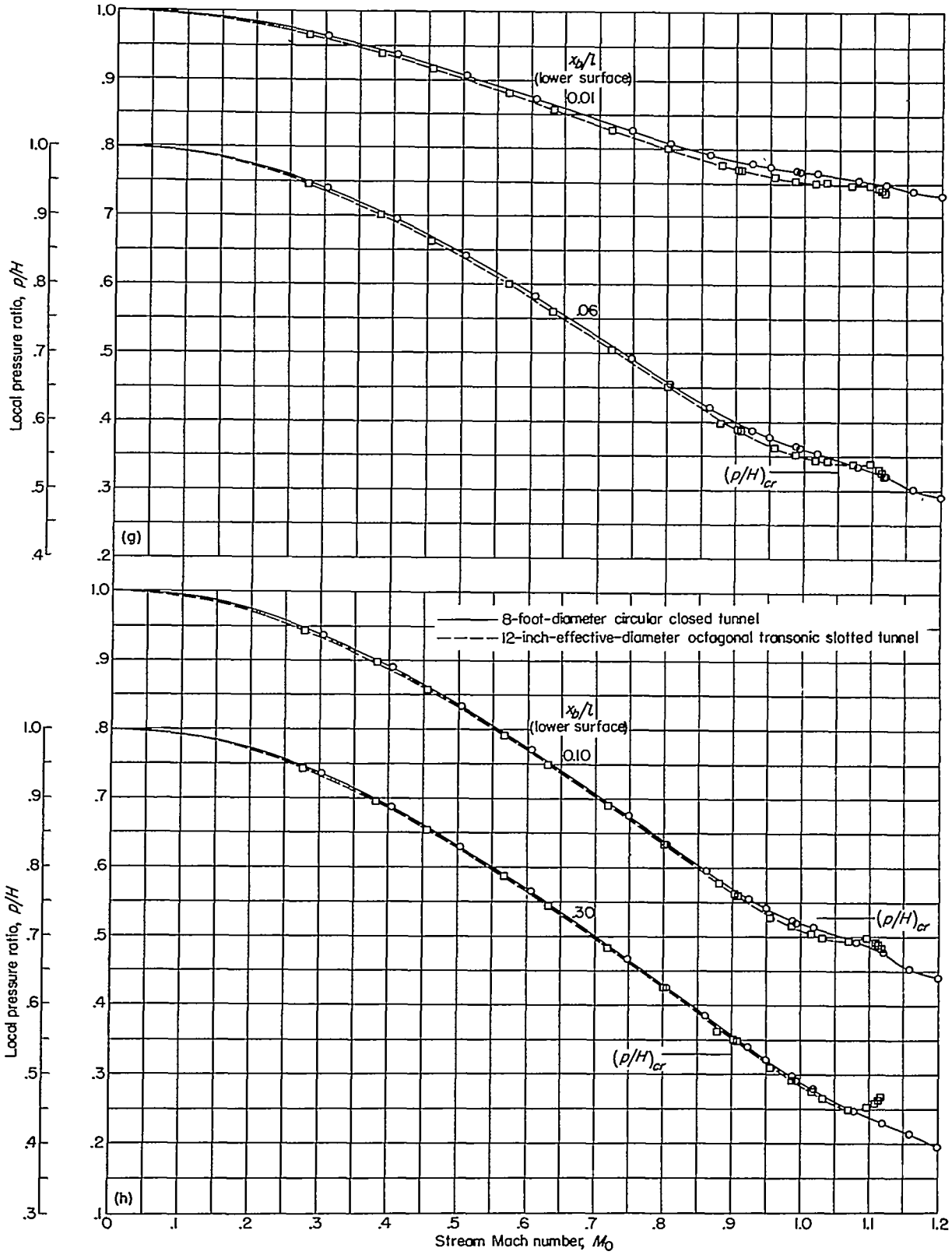

FIGURE 11.—Continued.

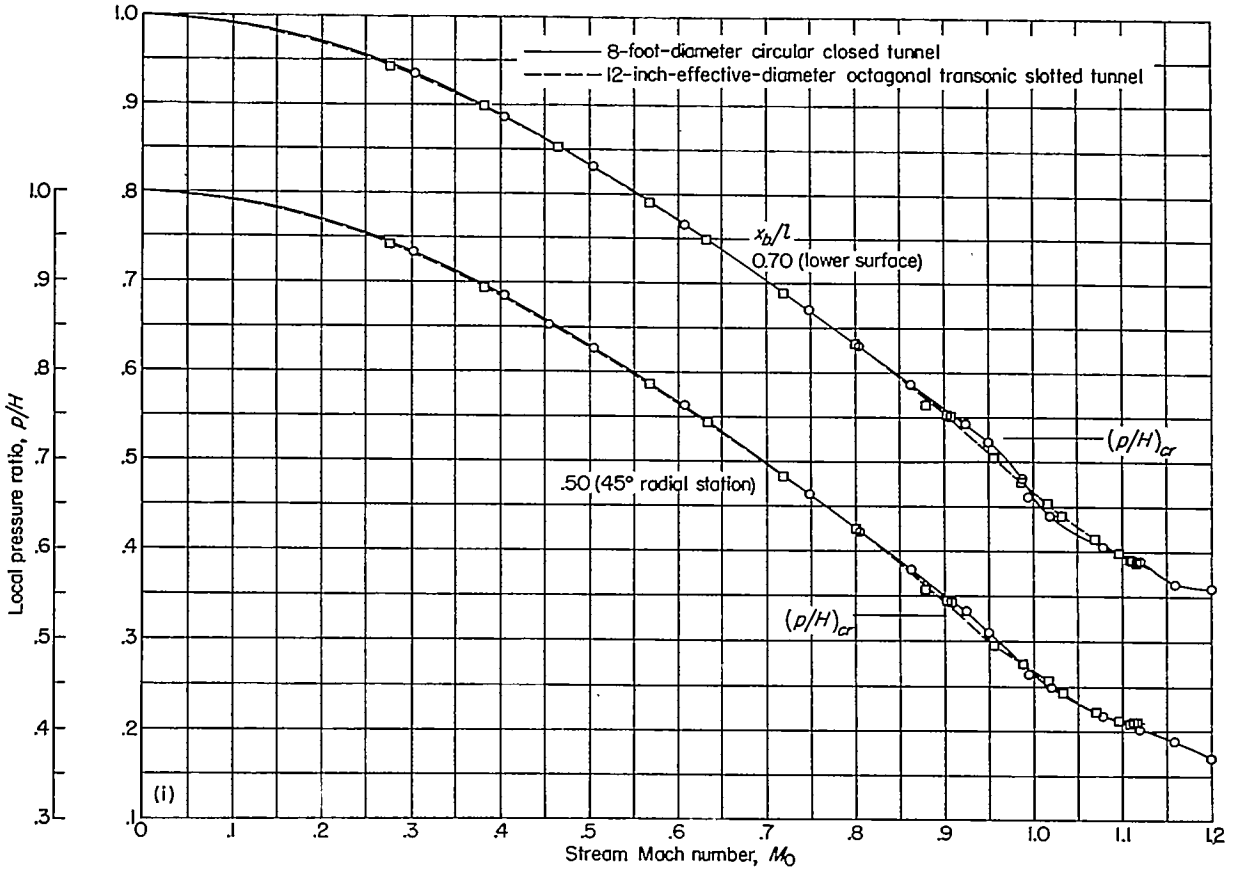

FIGURE 11.—Concluded.

Figure 16 presents comparisons similar to those of figure 15 over the body with wing affixed symmetrically. Again the pressure rise over the forward portion of the body is illustrated at Mach number 1.120. For further comparison a test point at a Mach number of 1.200 in the transonic slotted tunnel has been added. The large negative Mach number gradient existing over the rear portion of the body for this test point (see fig. 10) increases the pressures beyond the body station $x_b/l=0.30$. The distributions presented are of necessity limited because of the small number of pressure orifices in this small body.

Figure 17 presents limited chordwise distributions on the NACA 65–010 wing mounted on the body. The pressure differences indicated for the two tunnel configurations occur mainly in the region on the airfoil where the local speed of sound has been exceeded. A clearer comparison of these differences can be noted in the individual pressure comparisons in figure 13.

Figure 18 presents a comparison of the spanwise distributions along the wing. The important pressure differences between the two tunnel configurations occur near a Mach number of 0.900. These differences may be more clearly seen in figure 14.

The flow phenomena, as viewed by the schlieren flow-visualization method, over the 1.333-inch-diameter prolate spheriod, with NACA 65–010 wing affixed symmetrically, are presented throughout the transonic range of the 12-inch-effective-diameter octagonal slotted tunnel in figure 19. The schlieren system used necessitated separate exposures for the front and rear of the test model. The test Mach numbers are therefore not obtained simultaneously for the front and rear portions of the model. The position of the wing relative to the body has been indicated by placing as accurately as possible the wing silhouette on the schlieren negatives. These schlieren observations were made early in the investigation in order to substantiate further the measured pressures over the body, and no particular attention was given to the photographic impressions. Consequently, the quality of the resulting photographs is poor. It is believed, however, that these photographs tend to portray the development of the flow phenomena for the configuration indicated. The flow about the body and wing is three dimensional and the interpretation of the schlieren photographs is therefore difficult; however, certain aspects of the flow phenomena are interesting as well as enlightening.

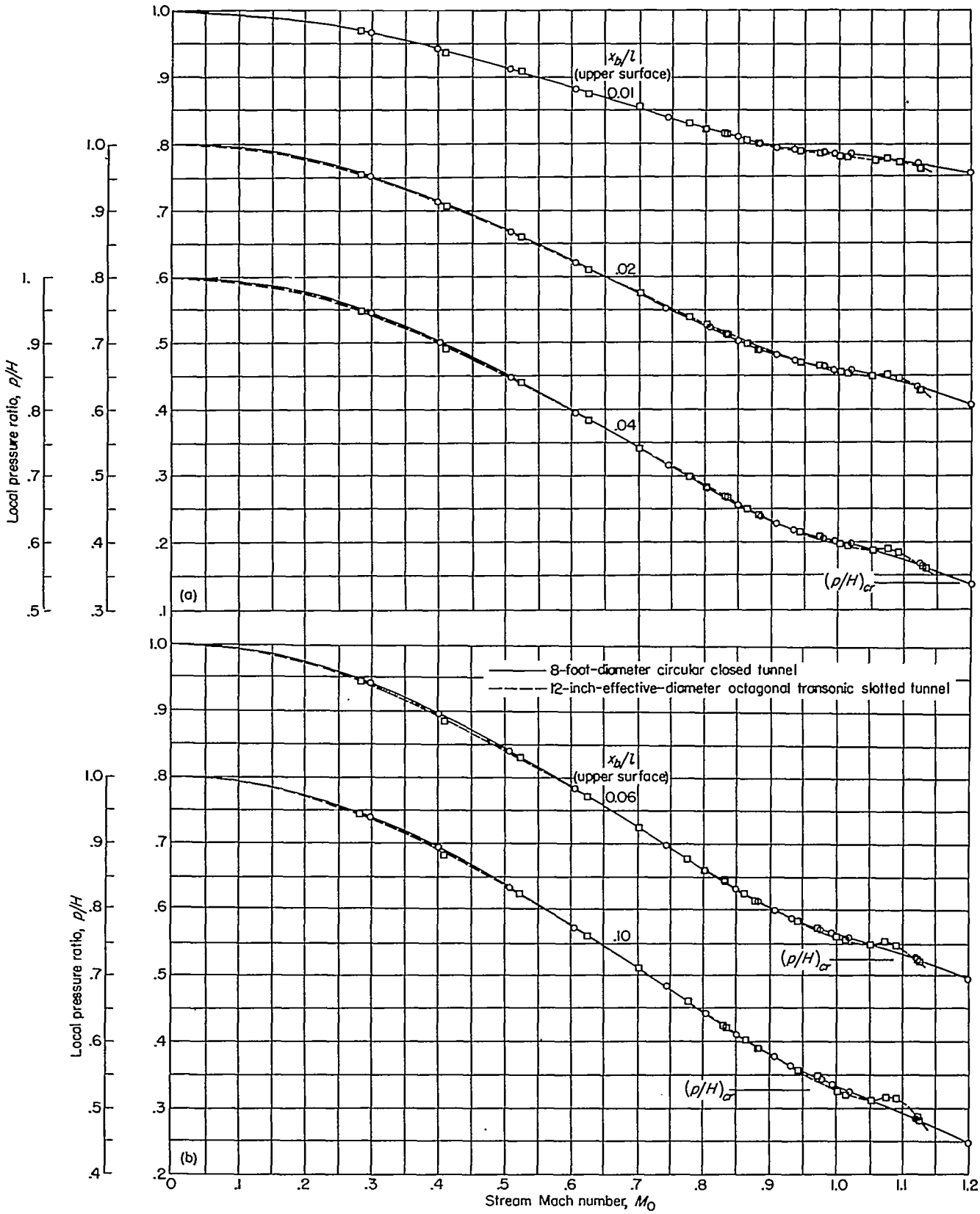

FIGURE 12.—Comparison of local pressures as a function of Mach number for several longitudinal stations along 1.333-inch-diameter prolate spheroid, with wing affixed symmetrically, in the transonic slotted tunnel and in a large closed tunnel.

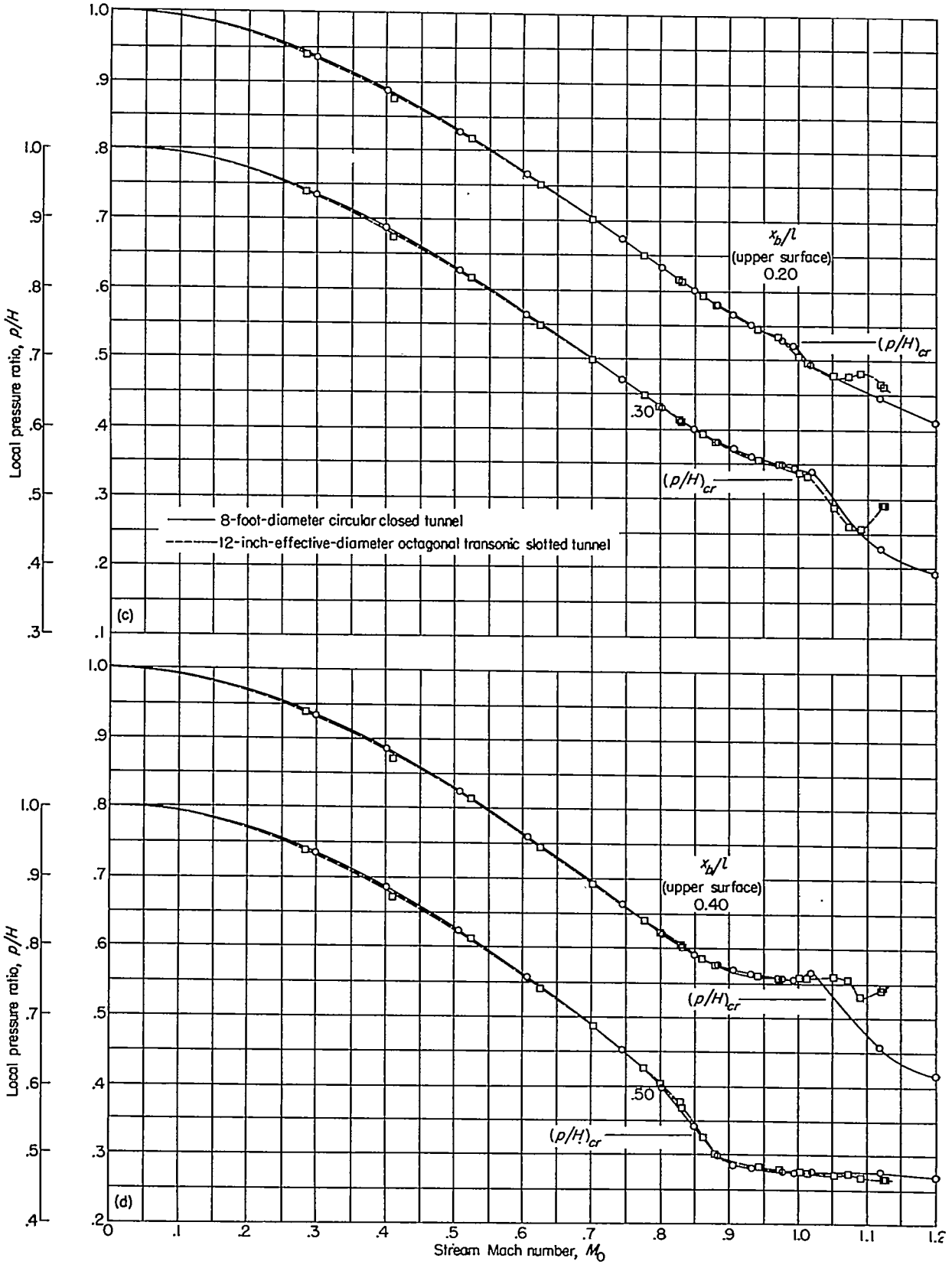

FIGURE 12.—Continued.

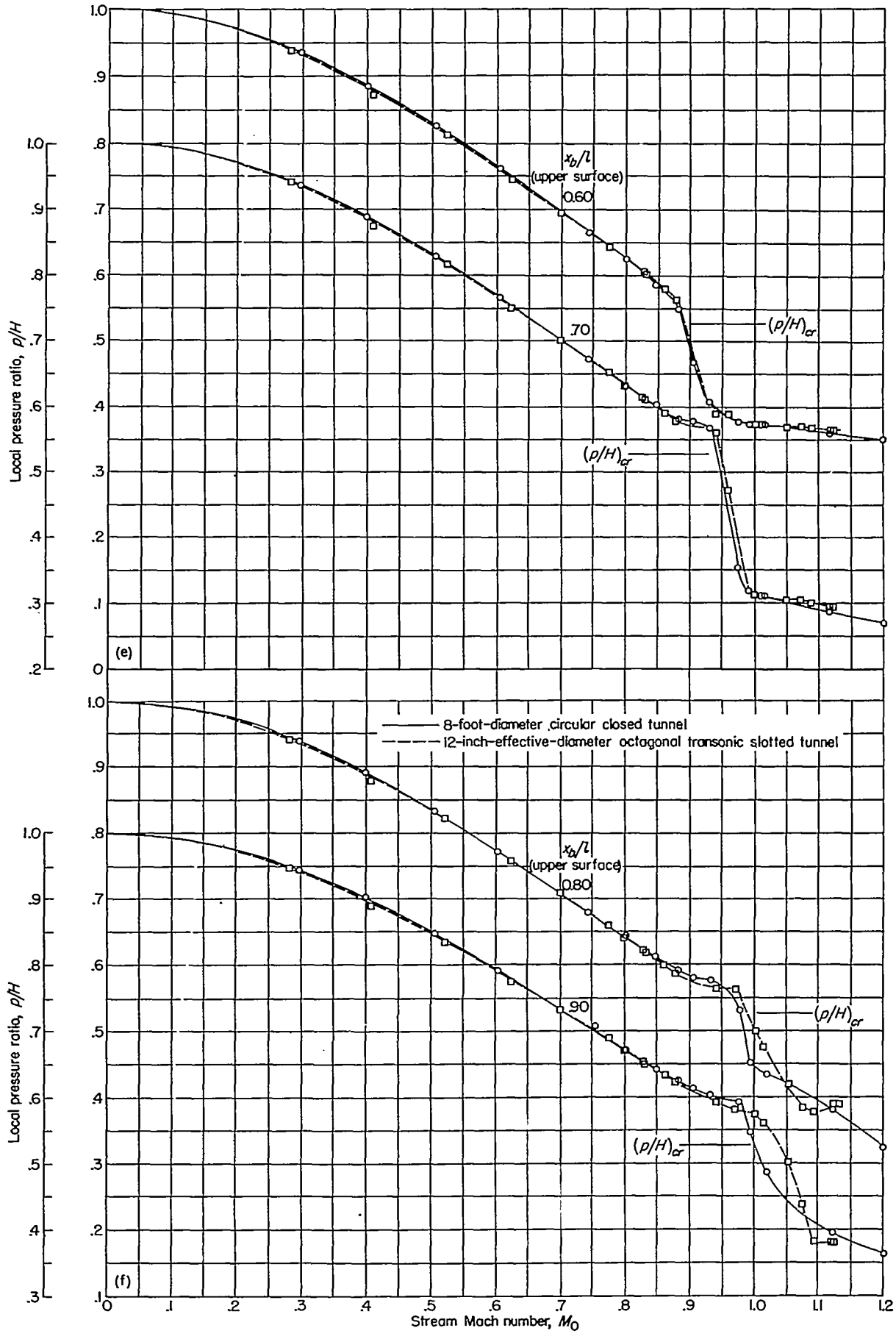

FIGURE 12.—Continued.

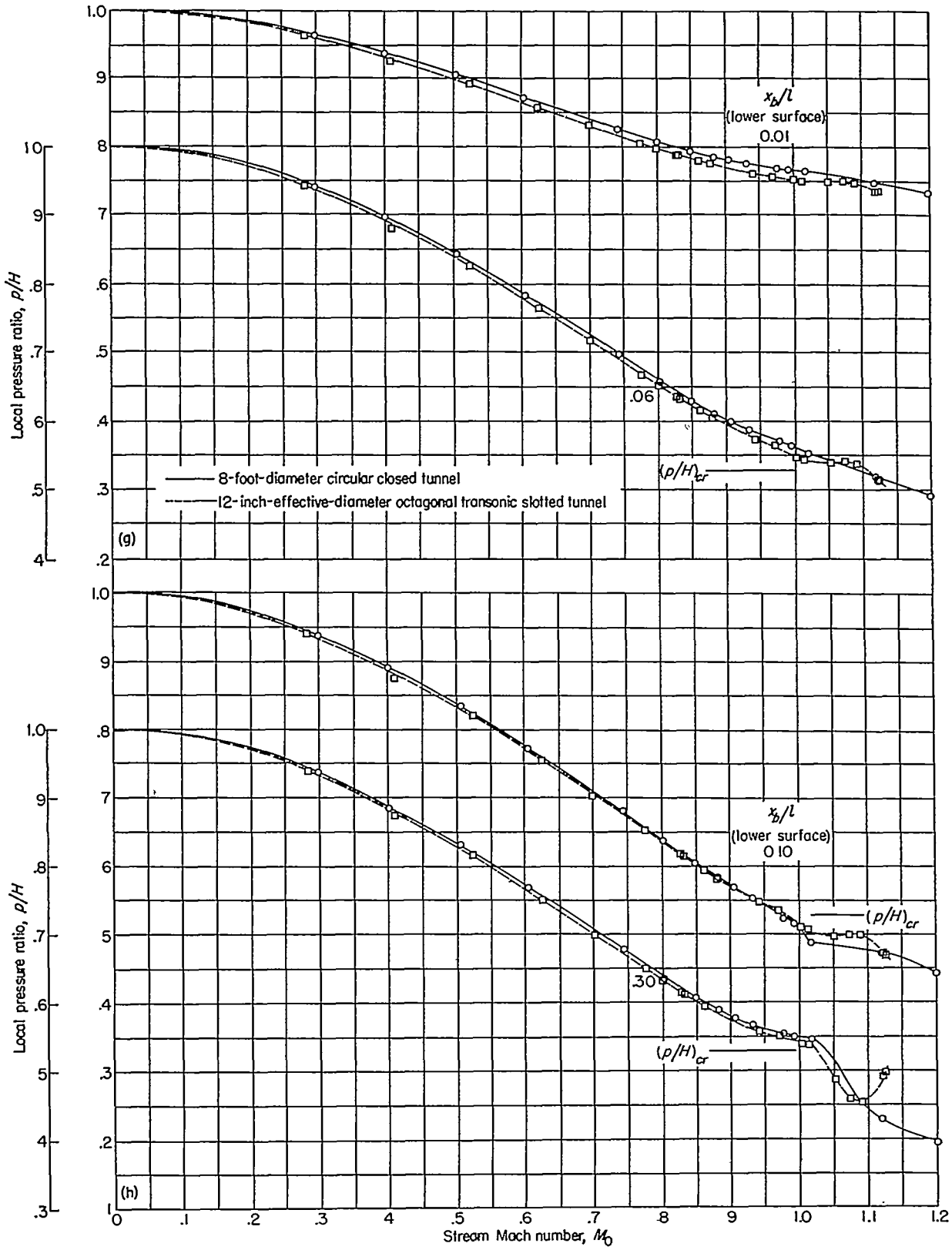

FIGURE 12.—Continued.

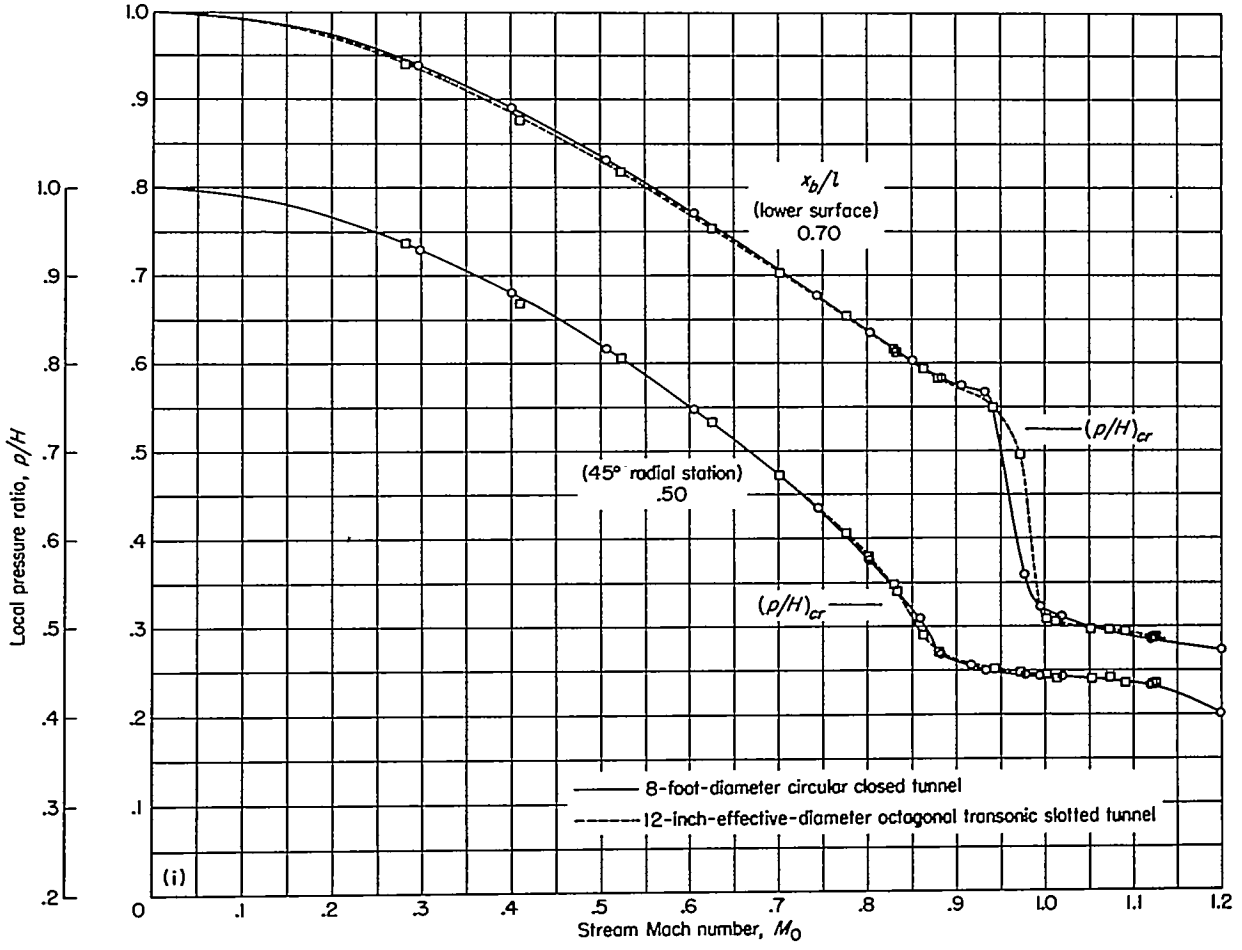

FIGURE 12.—Concluded.

The local supersonic region over the wing increases as the stream Mach number is increased until the shocks from the wing extend beyond the body and are visible at $M=0.86$ (figs. 19(a) and 19(b)). Increases in Mach number concentrate and move the almost two-dimensional wing shock rearward (figs. 19(c) and 19(d)) until at $M=0.94$ the shock appears to increase its angle with respect to a normal to the flow and to be nearly attached to the wing trailing edge. (See figs. 19(e) and 19(f).) A supersonic region also exists over the center of the body (fig. 16) and its three-dimensional shock is included in the combined disturbances at the trailing edge of the wing at Mach number approximately 0.97 (figs. 19(g) and 19(h)). A compression region exists on the body slightly forward of the wing. The following sudden expansion over the body is noted in the light region above the wing in figures 19(g) and 19(h).

At Mach number 1.00 a local supersonic region exists over the forward portion of the body, followed by an extremely light three-dimensional shock (fig. 19(i)). With further increase in Mach number the compression region at the rear of the body (figs. 19(j), 19(l), 19(n), 19(p), and 19(r)) expands rearward and eventually what appears to be a normal shock moves off the tail. The origin of this disturbance is at present unknown, nor is it known whether the phenomenon is characteristic of the body, of the tunnel configuration, or of the observational technique.

For Mach numbers near 1.0 the bow wave for the body has not appeared in the schlieren field (figs. 19(i) and 19(k)). At Mach number 1.01 (fig. 19(k)) a weak wing bow wave appears. As the Mach number is increased to 1.04 (fig. 19(m)), the wing bow wave increases in intensity. At these Mach numbers large movements of the bow waves occur for small changes in stream Mach number, and at Mach number 1.09 a strong bow wave has moved into the field of view ahead of the body (fig. 19(o)). A strong wing bow wave is also present in the schlieren field. The apparent abnormal width of the bow waves is due to three-dimensional curvature. The wing bow wave also possesses three-dimensional characteristics at the wing tips.

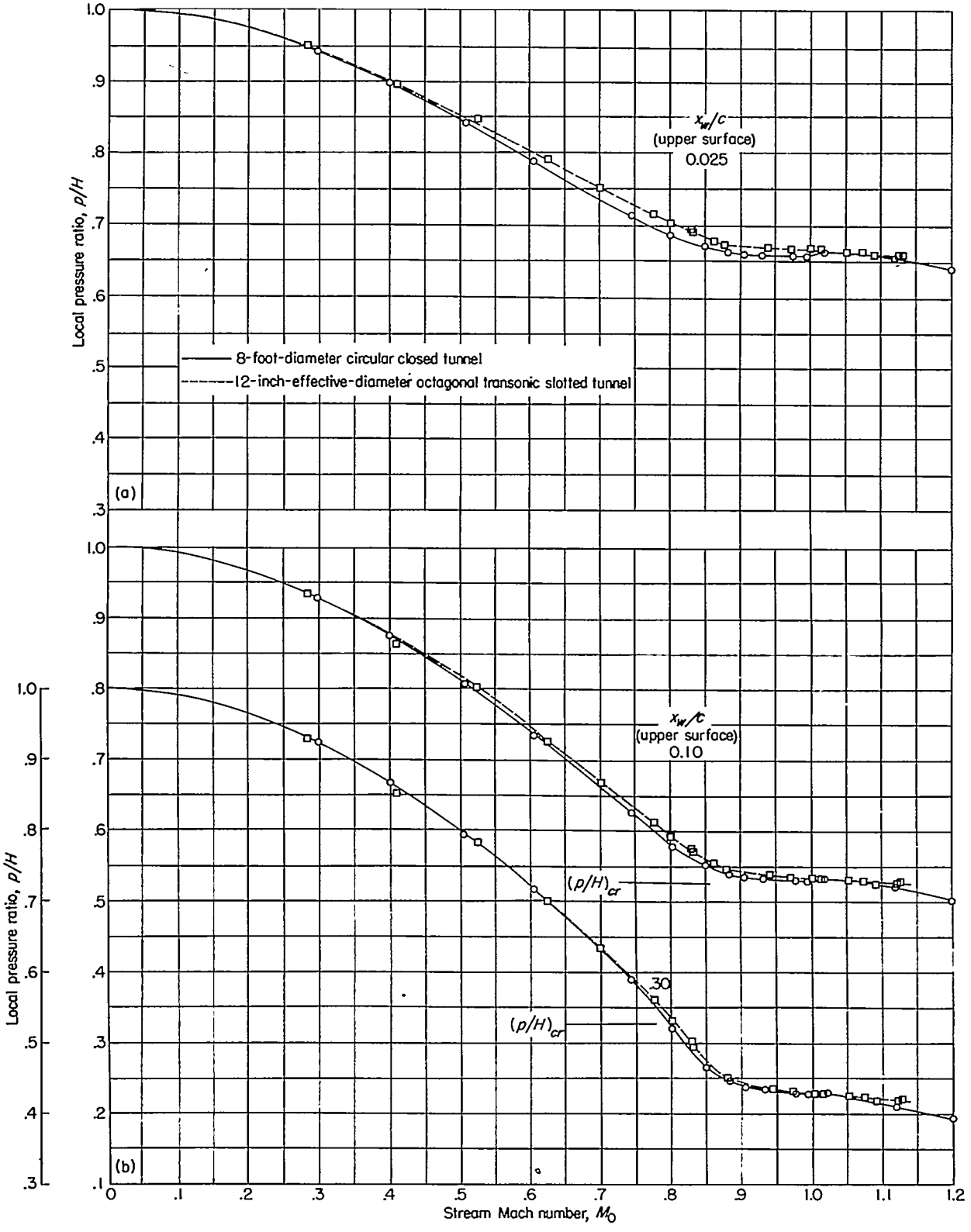

FIGURE 13.—Comparison of local pressures as a function of Mach number for several chordwise stations along the 61 percent semispan of NACA 65–010 wing affixed symmetrically on 1.333-inch-diameter prolate spheroid in the transonic slotted tunnel and in a large closed tunnel.

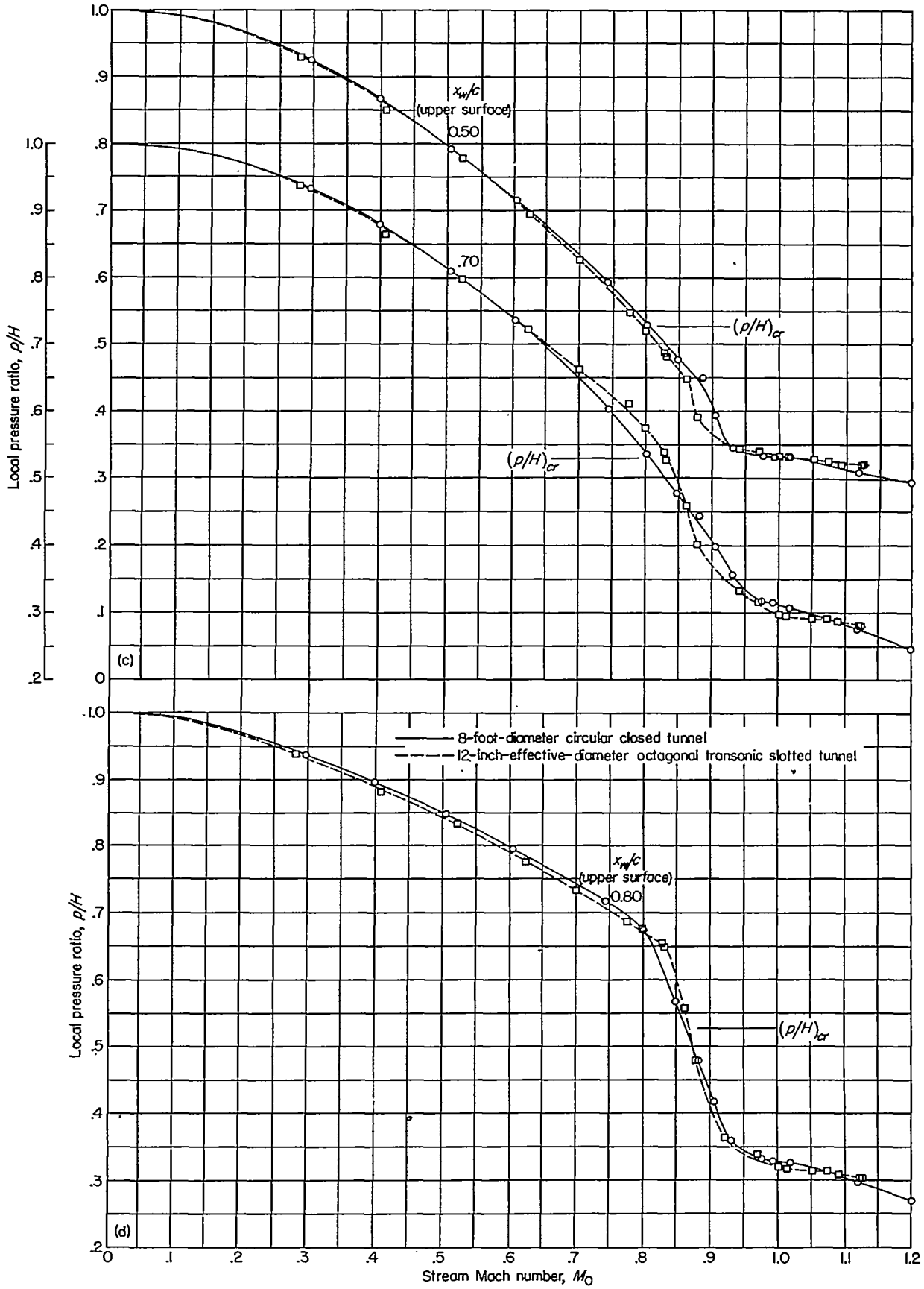

FIGURE 13.—Concluded.

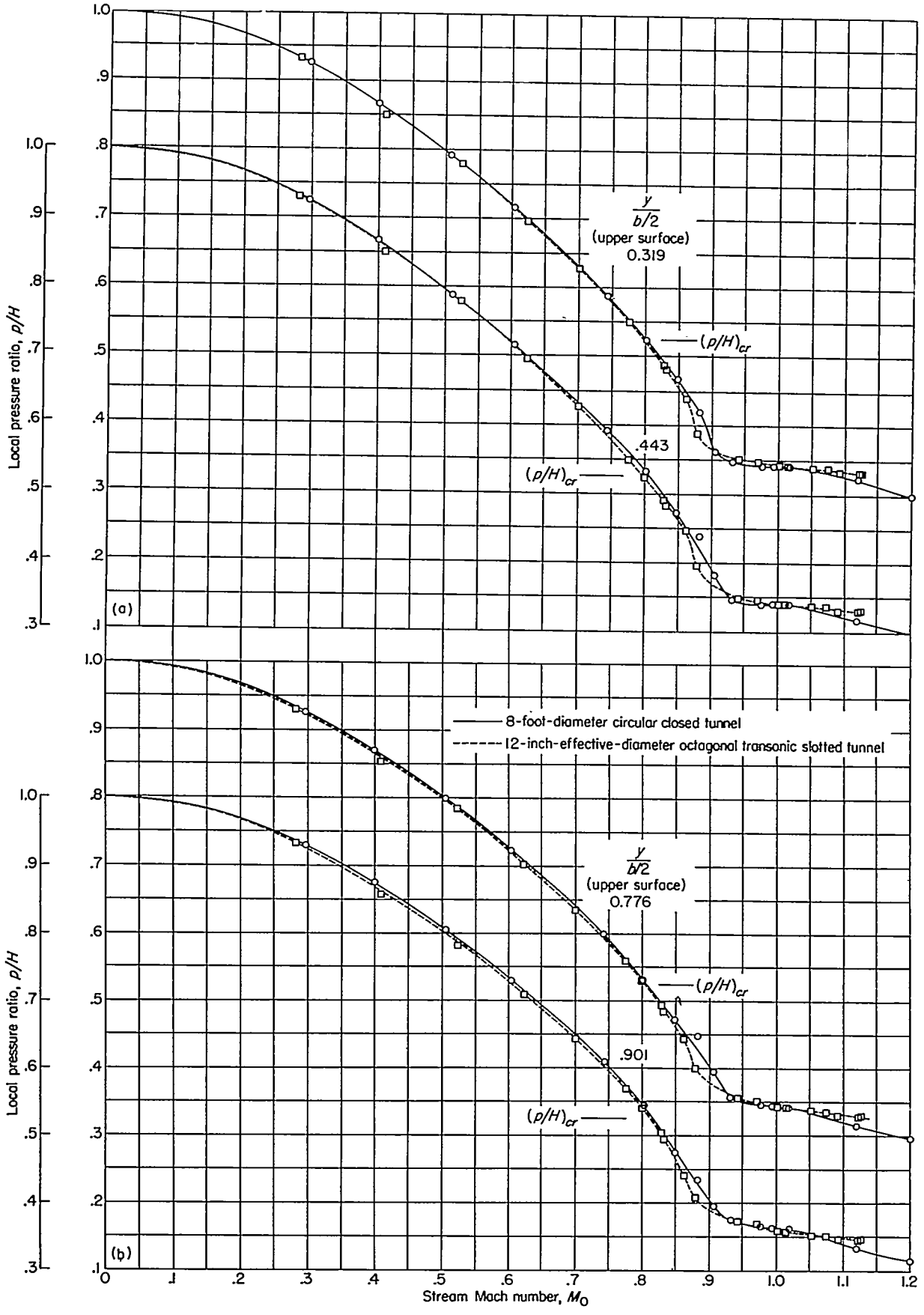

FIGURE 14.—Comparison of local pressures as a function of Mach number for several spanwise stations along the 50 percent chord of NACA 65–010 wing affixed symmetrically on 1.333-inch-diameter prolate spheroid in the transonic slotted tunnel and in a large closed tunnel.

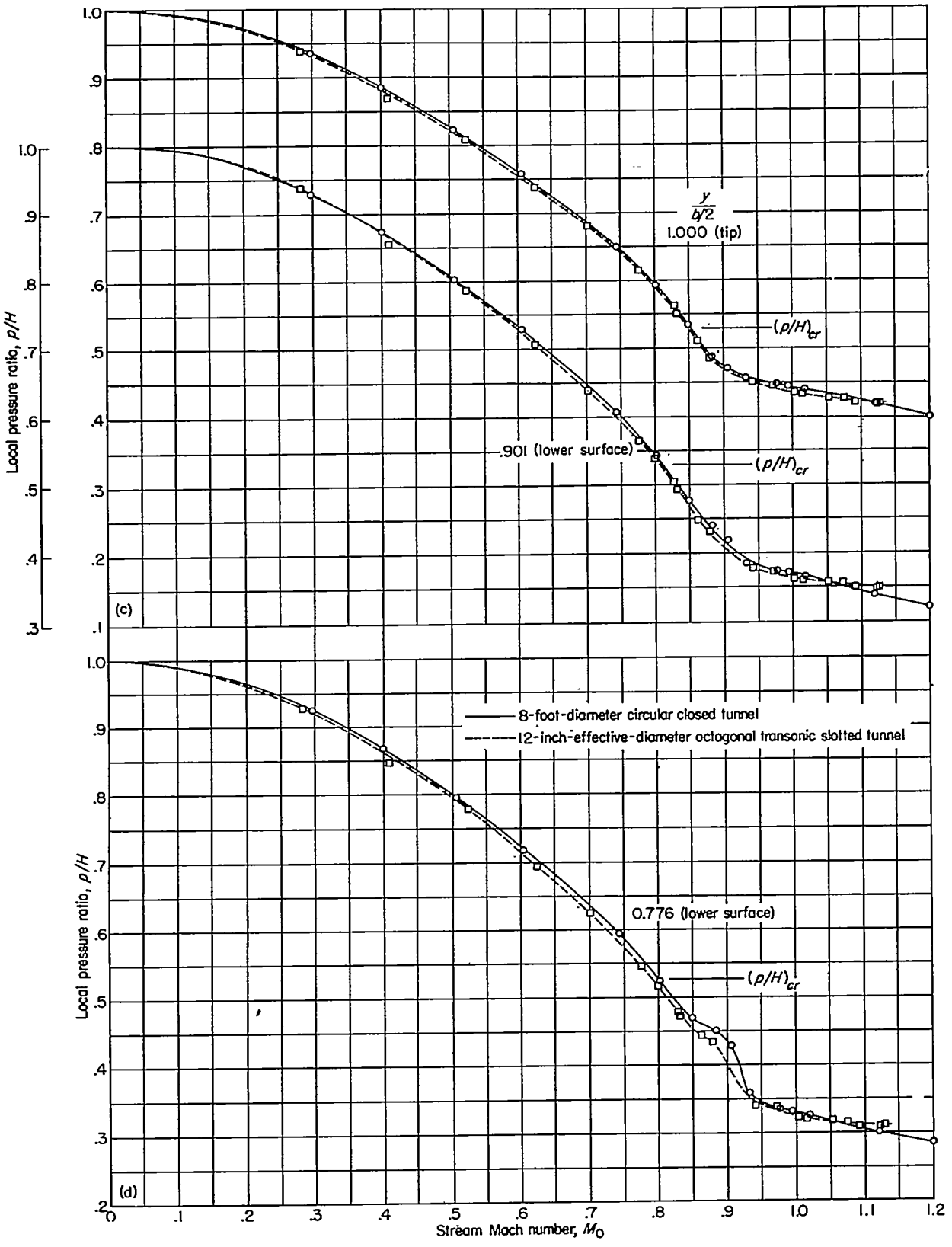

FIGURE 14.—Concluded.

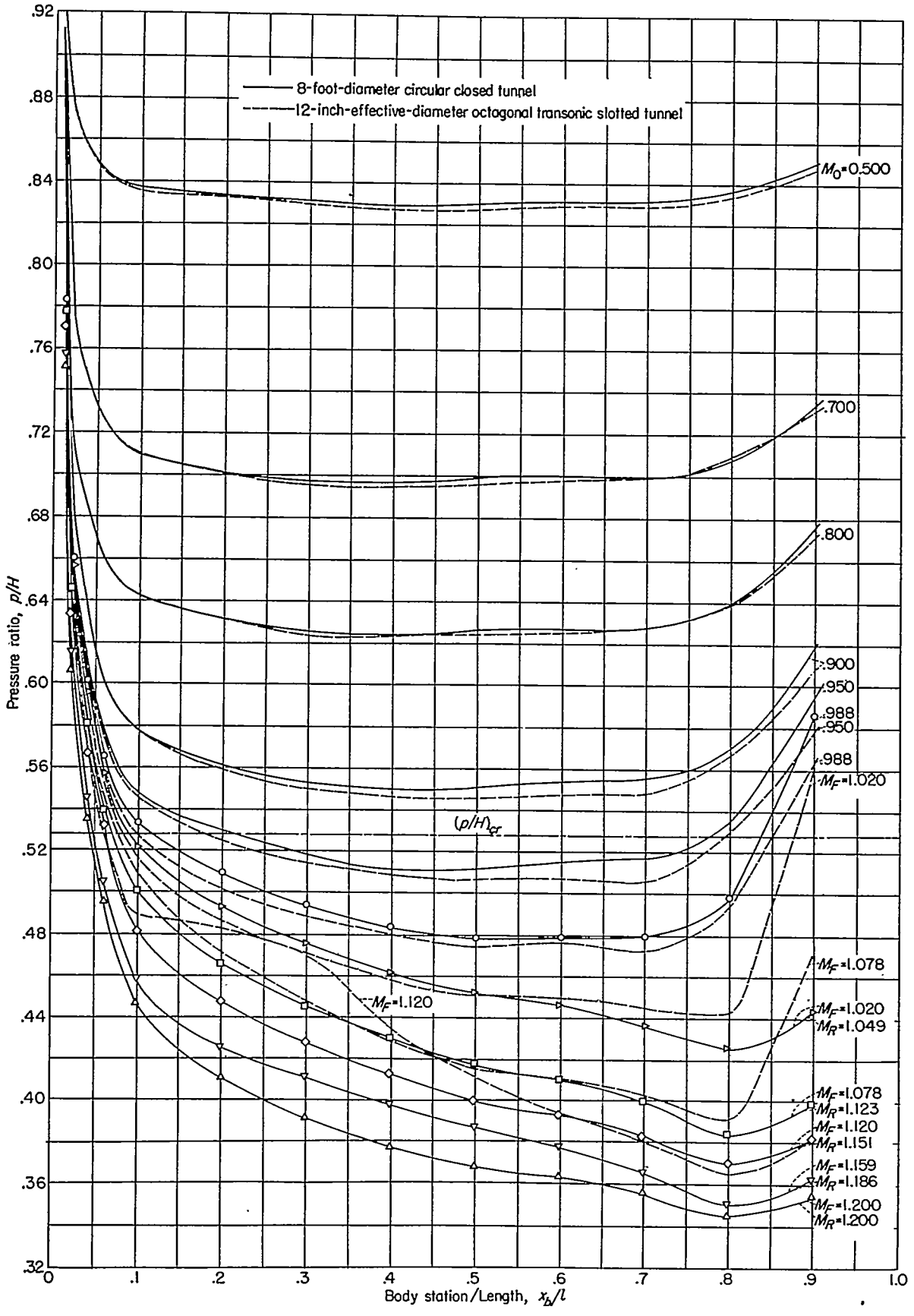

FIGURE 15.—Comparison of pressure distributions along top meridian of 1.333-inch-diameter prolate spheroid for several Mach numbers in the transonic octagonal slotted tunnel and in a large closed tunnel.

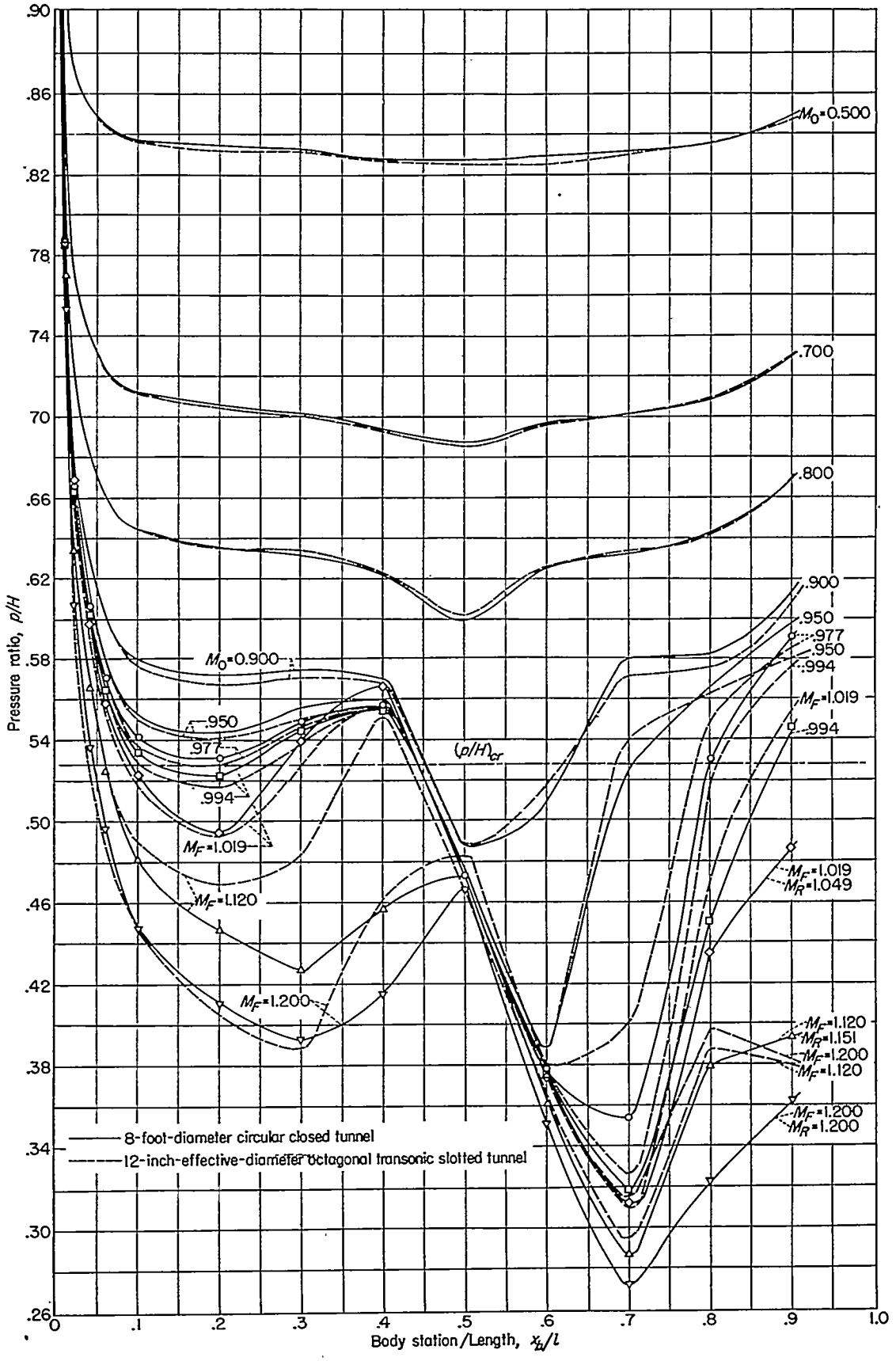

FIGURE 16.—Comparison of pressure distributions along top meridian of 1.333-inch-diameter prolate spheroid with wing affixed symmetrically for several Mach numbers in the transonic octagonal slotted tunnel and in a large closed tunnel.

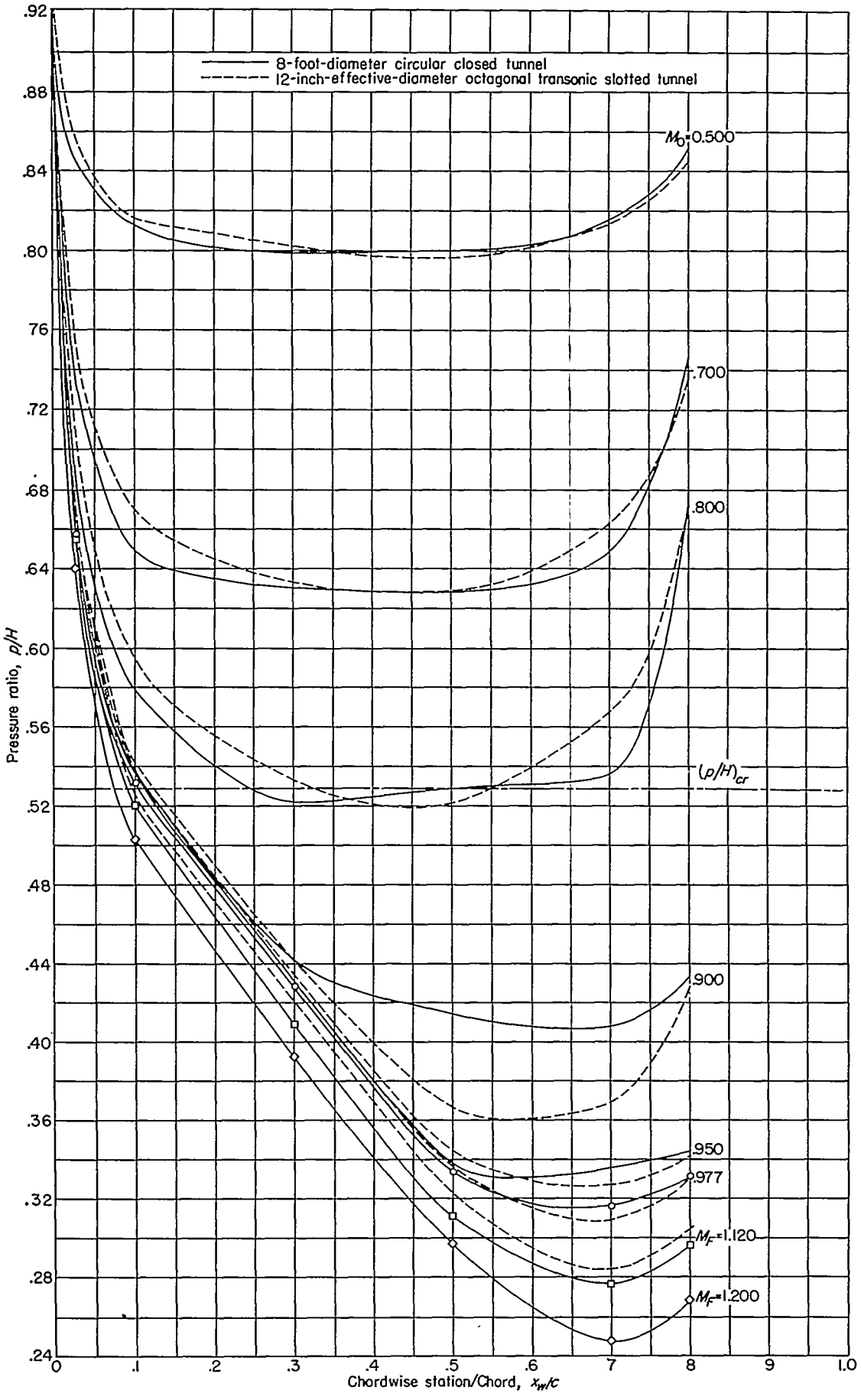

FIGURE 17.—Comparison of chordwise pressure distributions at 61 percent semispan of NACA 65–010 wing affixed symmetrically on 1.333-inch-diameter prolate spheroid, for several Mach numbers in the transonic octagonal slotted tunnel and in a large closed tunnel.

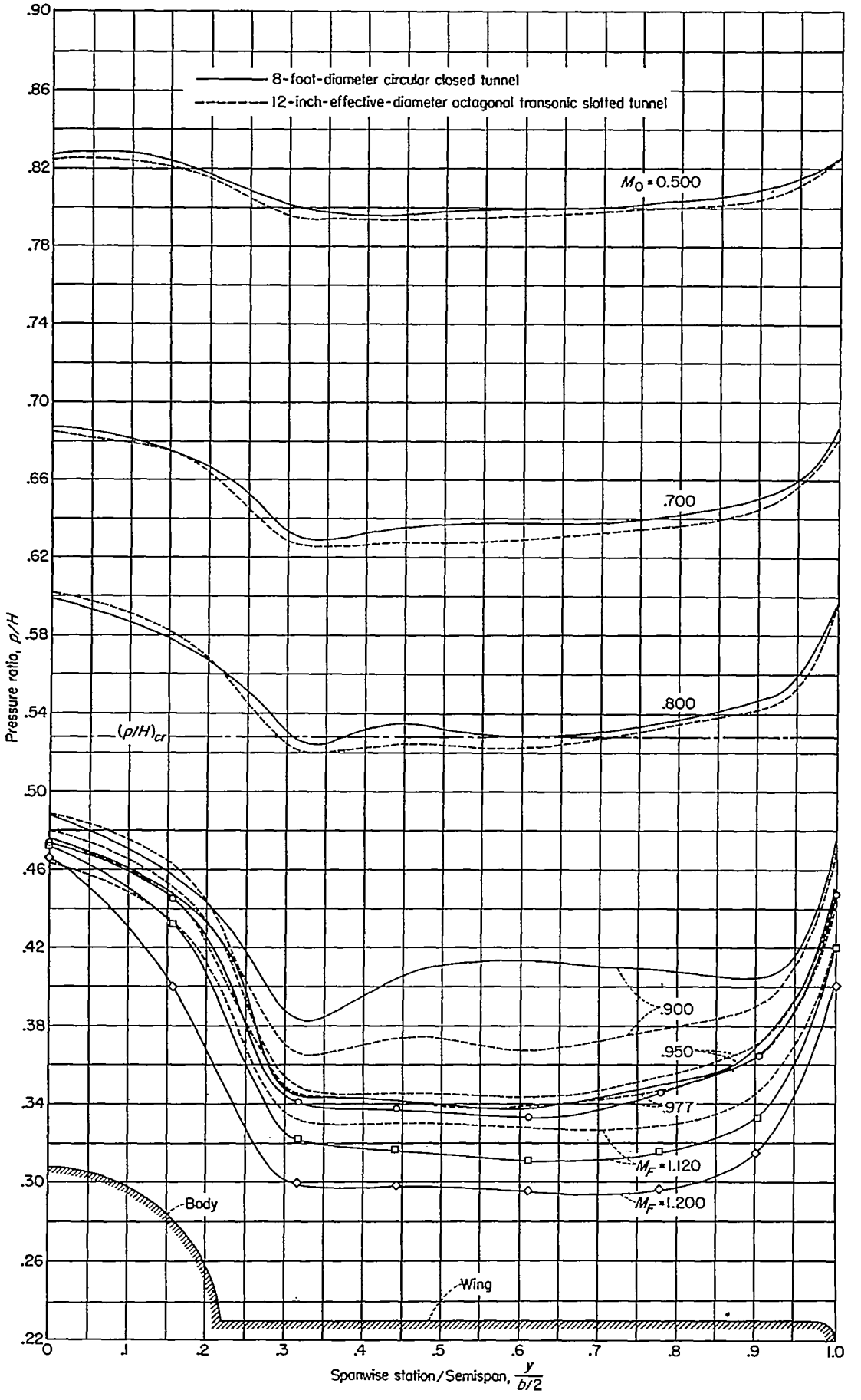

FIGURE 18.—Comparison of spanwise pressure distributions at 50 percent chord of NACA 65–010 wing affixed symmetrically on 1.333-inch-diameter prolate spheroid for several Mach numbers in the transonic octagonal slotted tunnel and in a large closed tunnel

(a) $M_0 = 0.86$.

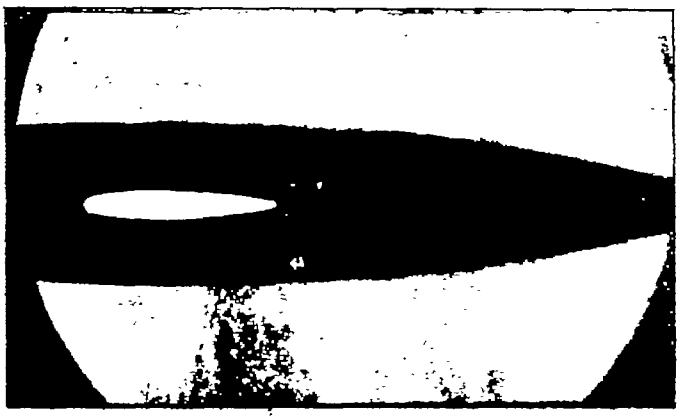

(b) $M_0 = 0.86$.

(c) $M_0 = 0.88$.

(d) $M_0 = 0.89$.

(e) $M_0 = 0.94$.

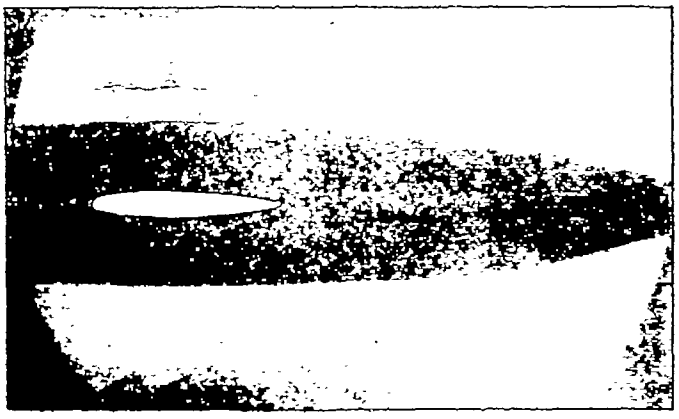

(f) $M_0 = 0.94$.

FIGURE 19.—Development of flow phenomena over 1.333-inch-diameter prolate spheroid with wing affixed symmetrically for increasing Mach number in 12-inch-effective-diameter octagonal transonic slotted tunnel.

(g) M_0=0.97.

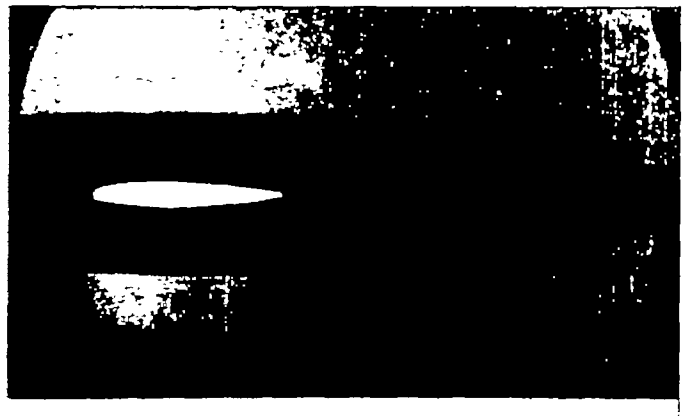

(h) M_0=0.98.

(i) M_0=1.00.

(j) M_0=1.00.

(k) M_0=1.01.

(l) M_0=1.01.

FIGURE 19.—Continued.

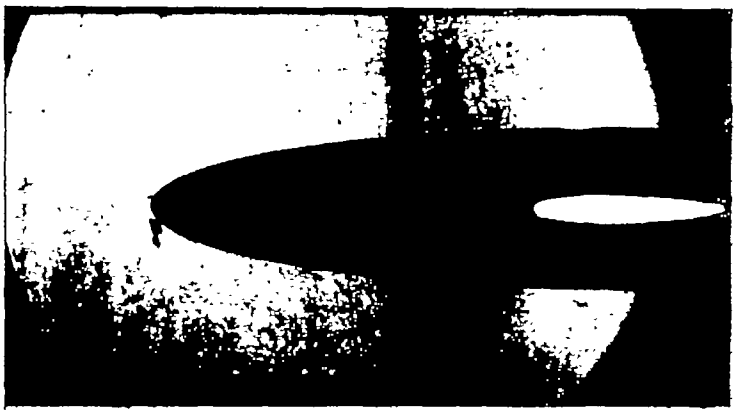

(m) $M_0 = 1.04$.

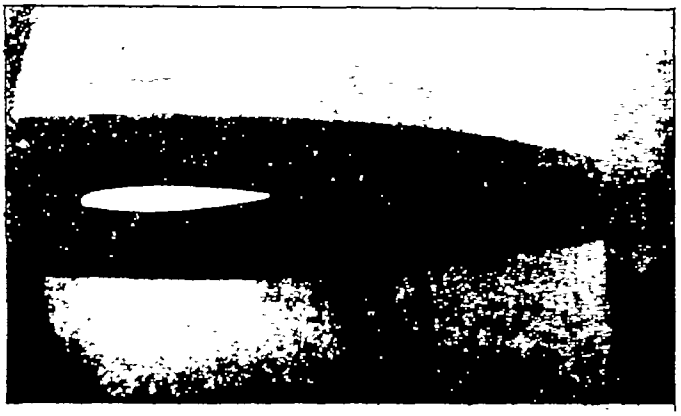

(n) $M_0 = 1.03$.

(o) $M_0 = 1.09$.

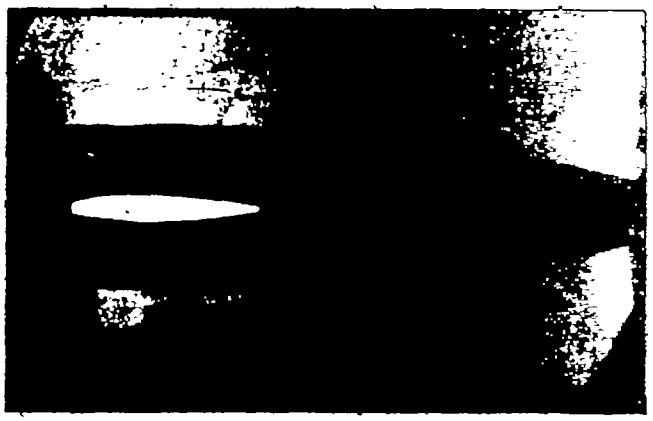

(p) $M_0 = 1.06$.

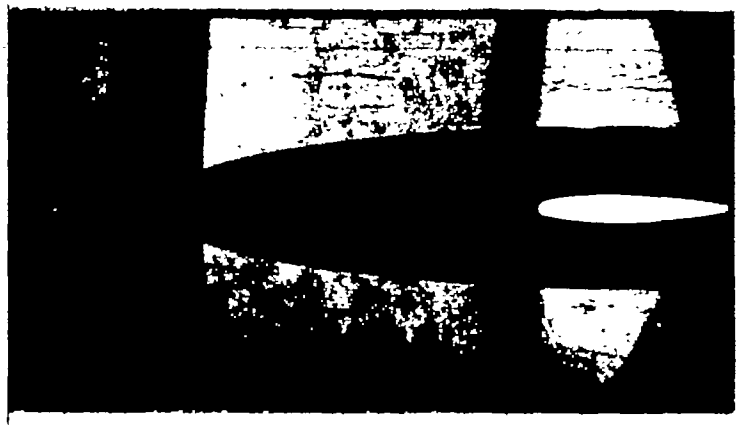

(q) $M_0 = 1.12$.

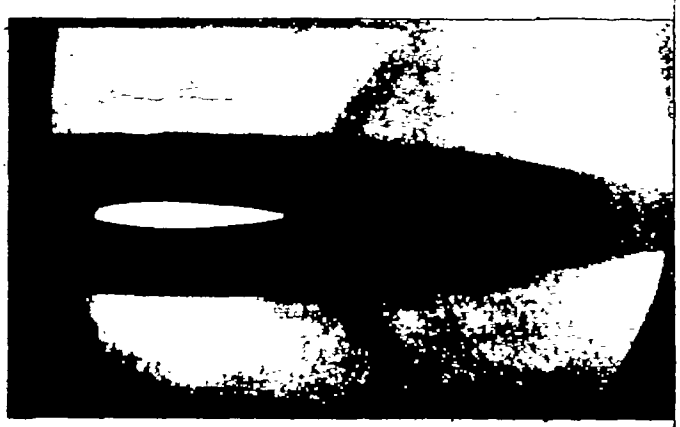

(r) $M_0 = 1.12$.

FIGURE 19.—Continued.

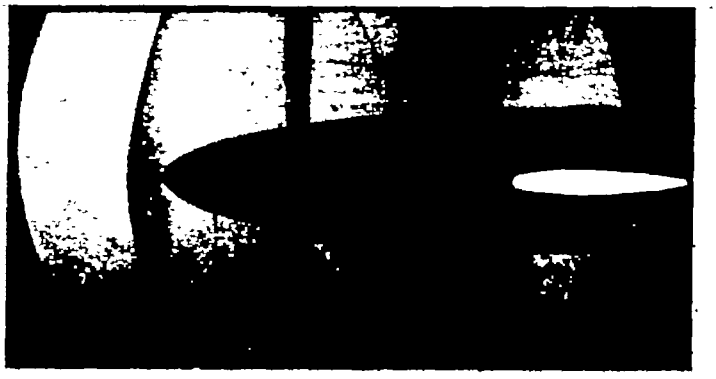

(s) M_0=1.14.

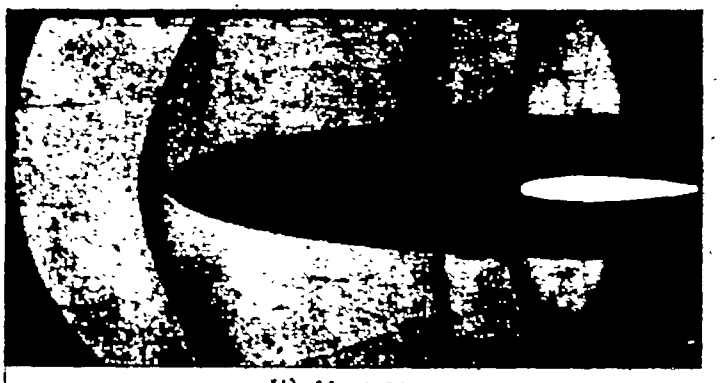

(t) M_0=1.21.

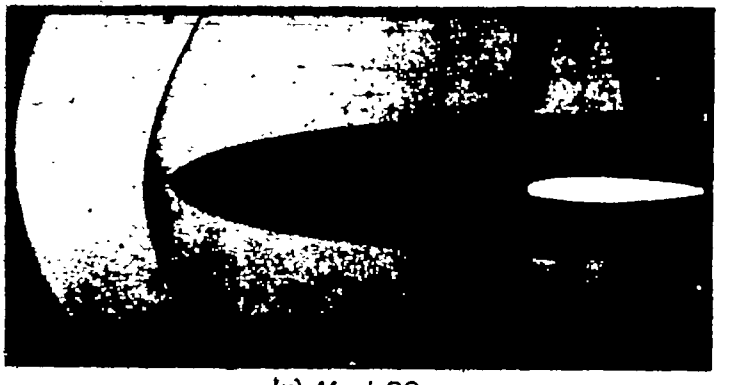

(u) M_0=1.22.

FIGURE 19.—Concluded.

At M=1.12 the three-dimensional aspects of the bow waves are apparent (fig. 19(q)). The intersection line caused by the flat schlieren windows produces the slight curvature at the rear of the wave.

At M=1.14 the only evidence of shock reflection occurs, and this reflection appears to originate from a point on the three-dimensional bow wave itself, rather than from the solid portion of the wall or from the slotted mixing region (fig. 19(s)). The intersection of the body bow wave with the schlieren windows is again noted behind the bow wave. The wing bow wave appears to move forward, probably on account of the negative Mach number gradient noted in the distributions with the slotted tunnel empty (fig. 10) for this Mach number. The losses in total pressure through the preceding waves may also exaggerate this effect.

At M=1.21 and 1.22, the bow-wave configuration ahead of the model has been definitely established, followed by its intersection lines on opposing schlieren windows (figs. 19(t) and 19(u)). The wing bow waves in figures 19(t) and 19(u) are probably not representative of the Mach number indicated, since the pressure ratios (fig. 16) obtained in the 12-inch-diameter slotted tunnel near this Mach number are in disagreement rearward of the 0.30 body station with those obtained in the 8-foot-diameter closed tunnel.

Figure 20 illustrates typical horsepower ratios for the 12-inch-effective-diameter transonic slotted tunnels and for the 12-inch-diameter open tunnel. The 12-inch-diameter closed tunnel operating supersonically with straight wall divergence is used as a base whereby an indication of relative horsepower in the open and slotted configuration is obtained. Actually, this basis for comparison tends to give power estimates too high for the slotted tunnel in the transonic range because, for the closed tunnel as operated for this comparison, the effective test section was shorter than would normally be employed.

The experiments up to the present time have been confined to the problem of operation of such a throat through the Mach number 1.0 range, and no particular effort has been made to obtain optimum power performance.

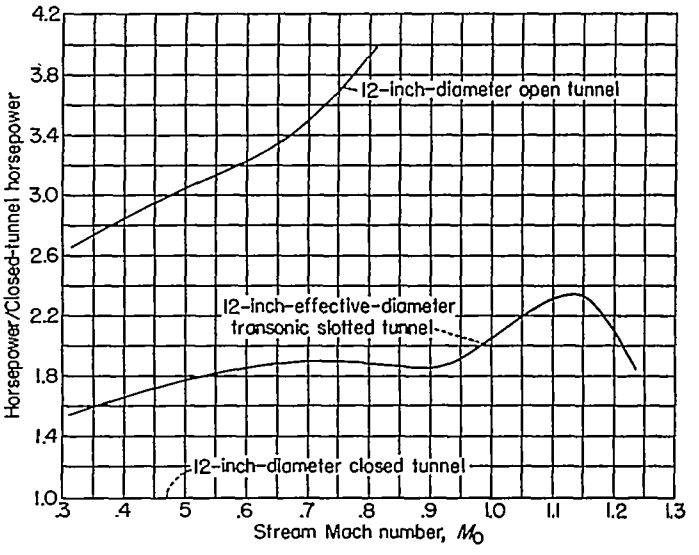

FIGURE 20.—Typical horsepower ratios as a function of Mach number for slotted and open tunnel configurations.

GENERAL DISCUSSION

As may be seen from figure 6, the principal prediction of the subsonic theory, in regard to minimization of the interference due to constriction of the tunnel walls by means of the circular 10-slot tunnel with one-eighth of the total periphery open, has been realized with the large 3.5-inch-diameter body. The Mach number to which the slotted tunnel can be satisfactorily operated is much greater than the choking Mach number in the closed tunnel. As seen in figure 7, the pressures at the center of the body appear to be approximately correct up to the highest Mach number obtained. With regard to the complete distribution over this large body, however, the slotted tunnel appears less satisfactory. As seen in figure 8, a distortion of the pressure diagram occurs, by which the pressures over the forward portion of the body are increased and those over the rear of the body are decreased. This distortion cannot be due to a pressure gradient in the empty tunnel because the pressure was essentially uniform over the test section. The subsonic theory based on potential flow about a symmetrical body cannot indicate any such asymmetrical distortion. The distortion indicated can be a result of too much outflow through the forward portion of the slots and may be due to interaction between the large body and the slots in the presence of the tunnel boundary layer. With a smaller model, therefore, the distortion should be reduced; and with the 1.333-inch-diameter body, which was less than half the size of the model used in the preliminary tests, this distortion in the subsonic range was not apparent. (See fig. 15.) With regard to angular variations, pressures measured at various angular stations around the center of the large body showed no detectable variations due to the slots.

With Mach numbers less than unity, the Mach number distribution in the test section of the transonic slotted wind tunnel is quite satisfactorily uniform, as may be seen for the wall and center-line positions from figures 5 and 10. With a Mach number greater than unity, the distribution becomes progressively less satisfactory as the Mach number is increased. Up to a Mach number of 1.1, however, the variations are not greater than might be expected in a closed tunnel, a conclusion that has been substantiated by schlieren observations, which show no sharp disturbances in the flow. The slotted tunnel presents the great advantage that the supersonic Mach number may be changed simply by varying the power input to the tunnel.

As seen in figures 11 to 18, models may be tested in the transonic slotted tunnel throughout the range of Mach numbers about 1.0. The test limitation due to choking has been eliminated, a fact that has been confirmed by schlieren photographs (fig. 19), which show progressive changes about the whole model throughout the transonic range. Over most of the model surface the correctness of the pressures, as indicated by comparison with results from the 8-foot tunnel, is fairly satisfactory. The relative pressure increase over the forward portion of the body at Mach numbers above 1.08 is believed to be due to some type of tunnel-wall interference. The disagreement with the 8-foot-tunnel results at the tail of the model may be due to the difference in Mach number gradients in this region, since for all supersonic Mach numbers less than 1.2 in the 8-foot tunnel, the model was tested in a positive Mach number gradient of about 0.03 over the length of the model, whereas, in the slotted tunnel, a negative gradient sometimes existed. If the flow over the rear of the model were critical, large differences in pressure might therefore exist. Similar differences might occur because of the Reynolds number and turbulence differences in the two tunnels. On the other hand, the operation of the slotted tunnel may be such as to exert an interference effect over the rear of the model.

The geometric design of the original circular slotted tunnel was intended to represent the boundary conditions assumed in the theory. The geometric minimum occurred two inches ahead of the upstream end of the slots, and the divergence downstream through the test section was only sufficient to compensate for the boundary layer that would be developed in a closed tunnel. The entrance lip at the upstream ends of the slots was made sharp so as to insure clean separation of the flow at this point. (See fig. 4(a).) The edges of the slots were rounded and the material behind the solid portions was cut away from behind the slots to insure constant potential at the slot positions (fig. 4(b)). These last two refinements were not adhered to in designing the octagonal slotted tunnel (fig. 4(c)). Otherwise the characteristics of the slotted tunnels are given in table II. The test section was made long, both because a large body for which the interference would be appreciable was to be tested and because the theory assumed an infinitely long cylindrical test section. The size of the tank was governed by consideration of space available and by probable interference effects. Downstream of the slotted test section, a slotted diffuser portion faired into the effuser bell at its juncture with the solid diffuser. At this point the cross-sectional area was about 20 percent greater than the upstream minimum area. The area ratio between downstream and upstream closed sections may be somewhat too large but experience has indicated that the highest supersonic Mach number obtained depends on this ratio. With subsonic operation, too small an area ratio results in tunnel choking at the downstream effective minimum before a Mach number of unity has been obtained in the test section.

The power required (see fig. 20) would be less with a shorter slotted test section. With somewhat wider slots than those used in the tests reported herein, essentially open tunnel operation could be obtained, at least for subsonic Mach numbers, with a considerable reduction of power as compared with that required for the completely open tunnel of the same length. The power also depends upon the ratio of the area at the beginning of the closed diffuser to that of the upstream minimum. It appears desirable to shorten the slotted test section in order to reduce the power. Such a modification may have practical limits with supersonic operation, because a certain test section length is required for the flow to settle out into a fairly uniform Mach number distribution. (See fig. 10.)

This investigation has demonstrated the possibility of reducing the solid-blockage interference and eliminating the

choking limitations of conventional wind tunnels. It therefore appears possible not only to test models larger than those usually employed in a wind tunnel of given size but also to cover a near-unity test Mach number range not heretofore practicable in wind tunnels. Further advantages include power consumption considerably less than that required for the open tunnel, and the possibility of controlling the Mach number at supersonic as well as subsonic speeds merely by varying the power. The practical realization of these advantages depends on the future development of the slotted wind tunnel.

CONCLUSIONS

On the basis of the data herein reported, the following conclusions are believed justified:

1. The interference due to solid blockage in a wind tunnel operating at subsonic speeds can be minimized by means of a slotted test section.
2. The closed-tunnel choking limitation can be eliminated by means of the slotted test section.
3. A slotted wind tunnel can be operated at low supersonic speeds merely by increasing the power, and the supersonic Mach number can be varied continuously by varying the power.
4. Test regions with satisfactorily uniform Mach number distribution can be obtained in the slotted test section at all subsonic speeds and at supersonic Mach numbers up to at least 1.1.
5. Pressure-distribution data obtained from tests of a nonlifting body in a slotted test section with the ratio of cross-sectional area of the body to cross-sectional area of the tunnel of 0.0123 show good agreement, up to Mach numbers somewhat exceeding the critical, with data for the same body obtained from tests in a closed tunnel for which the corresponding area ratio is 0.00019. For high Mach numbers including passage through Mach number 1.0, divergences of the two sets of data appear to occur, but reasonably good agreement is obtained over most of the model surface.
6. The transonic operation of this type of test section requires further experimentation and analysis before designs can be undertaken with certainty of complete adequacy. Particularly are data required for models of large lift. The power performance and the fundamental factors affecting power performance also require further study.

Langley Aeronautical Laboratory,
National Advisory Committee for Aeronautics,
Langley Field, Va., *June 20, 1955.*

REFERENCES

1. Churchill, Ruel V.: Modern Operational Mathematics in Engineering. McGraw-Hill Book Co., Inc., 1944, pp. 272–274.
2. v. Baranoff, A.: Tunnel Correction for Compressible Subsonic Flow. NACA TM 1162, 1947.
3. Gray, Andrew, Mathews, G. B., and MacRobert, T. M.: A Treatise on Bessel Functions and Their Applications to Physics. Second ed., Macmillan & Co., Ltd., 1931.
4. Watson, G. N.: A Treatise on the Theory of Bessel Functions. Second ed., The Macmillan Co., 1944, p. 172.
5. Wieselsberger, Carl: Über den Einfluss der Windkanalbegrenzung auf den Widerstand insbesondere im Bereiche der kompressiblen Strömung. Luftfahrtforschung, Bd. 19, Lfg. 4, May 6, 1942, pp. 124–128.
6. Hess, Robert V., and Gardner, Clifford S.: Study by the Prandtl-Glauert Method of Compressibility Effects and Critical Mach Number for Ellipsoids of Various Aspect Ratios and Thickness Ratios. NACA TN 1792, 1949. (Supersedes NACA RM L7B03a.)
7. Matthews, Clarence W.: Pressure Distributions Over a Wing-Fuselage Model at Mach Numbers of 0.4 to 0.99 and at 1.2. NACA RM L8H06, 1948.
8. Chapman, Dean R., and Perkins, Edward W.: Experimental Investigation of the Effects of Viscosity on the Drag of Bodies of Revolution at a Mach Number of 1.5. NACA Rep. 1036, 1951. (Supersedes NACA RM A7A31a.)